

Lawrence Berkeley National Laboratory

LBL Publications

Title

Anthropogenic Influences on Tornadic Storms

Permalink

<https://escholarship.org/uc/item/2hf7z8hq>

Journal

Journal of Climate, 34(22)

ISSN

0894-8755

Authors

Bercos-Hickey, Emily

Patricola, Christina M

Gallus, William A

Publication Date

2021-08-20

DOI

10.1175/jcli-d-20-0901.1

Copyright Information

This work is made available under the terms of a Creative Commons Attribution-NonCommercial License, available at <https://creativecommons.org/licenses/by-nc/4.0/>

Peer reviewed

Anthropogenic Influences on Tornadoic Storms

EMILY BERCOS-HICKEY,^a CHRISTINA M. PATRICOLA,^{b,a} AND WILLIAM A. GALLUS JR^b

^a *Climate and Ecosystem Sciences Division, Lawrence Berkeley National Laboratory, Berkeley, California*

^b *Department of Geological and Atmospheric Sciences, Iowa State University, Ames, Iowa*

(Manuscript received 23 November 2020, in final form 2 August 2021)

ABSTRACT: The impact of climate change on severe storms and tornadoes remains uncertain, largely owing to inconsistencies in observational data and limitations of climate models. We performed ensembles of convection-permitting climate model simulations to examine how three tornadoic storms would change if similar events were to occur in pre-industrial and future climates. The choice of events includes winter, nocturnal, and spring tornadoic storms to provide insight into how the timing and seasonality of storms may affect their response to climate change. Updraft helicity (UH), convective available potential energy (CAPE), storm-relative helicity (SRH), and convective inhibition (CIN) were used to determine the favorability for the three tornadoic storm events in the different climate states. We found that from the pre-industrial period to the present, the potential for tornadoic storms decreased for the winter event and increased for the nocturnal and spring events. With future climate change, the potential for tornadoic storms increased for the winter and nocturnal events in association with increased CAPE, and decreased for the spring event despite greater CAPE.

KEYWORDS: Climate change; Convective storms; Regional models


1. Introduction

Severe storms, defined as storms that produce tornadoes, straight-line winds of 50 kt (1 kt \approx 0.51 m s⁻¹) or more, and hail larger than 2.54 cm in diameter, were the leading cause of weather-related fatalities in the United States between 2009 and 2018 (NWS 2020). Tornadoic storms can also cause billions of dollars in damages (Brooks and Doswell 2001; Simmons et al. 2013; Allen 2018), demonstrating both the human and monetary costs of these extreme weather events. Given their deadly and destructive nature, it is crucial to understand what drives change and variability in tornadoic storms. However, the response of tornadoic storms to climate change has proven difficult to assess and remains uncertain (Brooks 2013).

One of the difficulties of research involving observational severe storms climatology stems from the limited availability of data. The severe storm and tornado observational record is nonuniform in space and time (Brooks et al. 2003a). Tornado databases have been subject to inconsistencies in the reporting system and changes in the population density (Brooks et al. 2003a; Verbout et al. 2006; Diffenbaugh et al. 2008; Doswell et al. 2009; Edwards et al. 2013). Additionally, global and regional climate models run at coarse horizontal grid spacing with convective parameterizations are not able to adequately resolve severe storms and tornadoes (Trapp et al. 2007; Tippett et al. 2015). To overcome these difficulties, studies have examined atmospheric environmental parameters that are often indicators of severe storm and tornado potential (Brooks et al.

1994; Trapp et al. 2007; Marsh et al. 2007), although these parameters are also sensitive to resolution, particularly in the vertical (Diffenbaugh et al. 2013; Gensini et al. 2014b). Environmental parameters are based on the two main ingredients for severe storms: instability and vertical wind shear (Brooks et al. 1994, 2003b; Doswell et al. 2012). Convective available potential energy (CAPE) and convective inhibition (CIN) (Colby 1984) are measures of instability that indicate the potential development or suppression of severe storms, respectively (Brooks et al. 1994; Rasmussen and Blanchard 1998). The 0–1-km bulk wind shear and 0–1-km storm-relative helicity (SRH) (Davies-Jones 1993) are measures that indicate potential updraft rotation and tornadoes (Brooks et al. 1994; Rasmussen and Blanchard 1998; Thompson et al. 2003, 2007). Tornadoic storm development is associated with low CIN, strong vertical wind shear, strong vertical lift environments, and low to high CAPE depending on the season and type of event (Rasmussen and Blanchard 1998; Thompson et al. 2003, 2012; Sherburn and Parker 2014).

Global and regional climate model data have been used to examine future changes in environments favorable for tornadoic storm development. Studies have found that the frequency of severe storms will increase due to an overall increase in favorable environmental parameters, mostly driven by increasing temperatures and moisture in the lower troposphere (Del Genio et al. 2007; Trapp et al. 2007; Diffenbaugh et al. 2008; Trapp et al. 2009; Diffenbaugh et al. 2013; Seeley and Romps 2014; Allen et al. 2014). Of these studies, some found a future decrease in vertical wind shear in response to a reduction in the equator-to-pole temperature gradient (Trapp et al. 2007; Del Genio et al. 2007; Trapp et al. 2009; Van Klooster and Roebber 2009). Diffenbaugh et al. (2013), however, showed that decreases in shear are mostly confined to days with lower instability, and thus will likely not have a significant impact on severe storm frequency. Additionally, Diffenbaugh et al. (2013) found future increases in occurrences of high mixed layer CAPE in

 Supplemental information related to this paper is available at the Journals Online website: <https://doi.org/10.1175/JCLI-D-20-0901.s1>.

Corresponding author: Emily Bercos-Hickey, ebercoshickey@lbl.gov

combination with high 0–1-km shear, both of which are important for tornado development (Thompson et al. 2003).

Although studies have used environmental parameters to show a future increase in favorability for tornadic storm development, this approach is not without limitations. Environmental parameters derived from coarse global and regional climate model data can be biased from the behavior of convective parameterization schemes (Marsh et al. 2007). Changes in environmental conditions also do not necessarily manifest in changes to unresolved tornadic storm events (Robinson et al. 2013; Hoogewind et al. 2017). Future increases in CAPE are often accompanied by future increases in CIN, adding to the uncertainty of inferring changes in severe storms and tornadoes from environmental parameters (Brooks 2013; Gensini and Mote 2015; Trapp and Hoogewind 2016; Rasmussen et al. 2017; Hoogewind et al. 2017). The limitations associated with environmental parameters have led to the increased use of dynamical downscaling, which eliminates the need for convective parameterizations (Allen 2018).

Gensini and Mote (2015) used high-resolution dynamical downscaling to examine a decade of hazardous convective weather in the historical and the late-twenty-first-century time periods. They found a significant future increase in both the frequency and variability of hazardous convective weather, most notably in the months of March and April. Using 13 years of historical and future dynamically downscaled simulations, Rasmussen et al. (2017) found a future increase in CAPE, in agreement with previous studies. However, they also found a future increase in CIN that acts as a balancing force such that there is a future decrease in the frequency of weak to moderate storms and a future increase in extreme storms. Hoogewind et al. (2017) examined both environmental parameters from global climate model data and simulated severe weather from high-resolution dynamical downscaling. They found a future increase in intensity and a lengthening of the severe storm season in both datasets. Hoogewind et al. (2017) noted that changes in the frequency of environments favorable for severe storms from the global climate model data were 2 to 4 times larger than those from the dynamical downscaling. These results highlight the limitations of global climate model-based environmental analysis and the need for high-resolution dynamical downscaling.

Given the limitations of environmental parameters, recent studies have utilized dynamical downscaling to examine specific tornadic storm events (Trapp and Hoogewind 2016; Molina et al. 2020; Carroll-Smith et al. 2020). Molina et al. (2020) used high-resolution, convection-permitting Weather Research and Forecasting (WRF) model simulations to examine the effects of sea surface temperatures on tornadic storms. They found that warmer sea surface temperatures in the Gulf of Mexico increase tornado frequency, which could have implications for future tornadic storm activity. To consider the effects of climate change, Trapp and Hoogewind (2016) and Carroll-Smith et al. (2020) used the pseudo-global warming (PGW) method, where a climate change difference is used to modify the initial and boundary conditions of the model (Schär et al. 1996). This method has been used to study heavy precipitation, tropical and extratropical cyclones, and

severe storms (Frei et al. 1998; Lackmann 2013, 2015; Trapp and Hoogewind 2016; Michaelis et al. 2017; Patricola and Wehner 2018; Carroll-Smith et al. 2020). Trapp and Hoogewind (2016) used the PGW method in combination with high-resolution, convection-permitting WRF simulations to examine three spring tornadic storms. Future realizations of the tornadic storms showed increased values of CAPE that had the potential to lead to strong convective updrafts, but the combined effects of CIN and decreased parcel lifting suppressed convective initiation (Trapp and Hoogewind 2016). Additionally, future increases in the thermodynamically induced updraft velocity were seen to be potentially overwhelmed by condensate loading (Trapp and Hoogewind 2016). The PGW method in combination with high-resolution, convection-permitting WRF simulations was also used to examine the relationship between tropical cyclone tornado-producing storms and climate change (Carroll-Smith et al. 2020). The PGW simulations showed an increase in tropical cyclone intensity and rainfall, but the effect on tornadic storms was inconclusive. Tornadic storm production, however, was found to be related to the tropical cyclone track length in addition to favorable environmental conditions (Carroll-Smith et al. 2020).

Although progress has been made on how severe storms and tornadoes will respond to climate change, critical knowledge gaps and uncertainty remain. Previous studies have often relied on simulations with parameterized convection and resolution too coarse for evaluating convective storms and their features (Trapp et al. 2009; Diffenbaugh et al. 2013; Seeley and Romps 2014; Gensini et al. 2014a). Studies that utilize dynamical downscaling allow for the analysis of storm-scale parameters, but relatively few studies have examined the effects of climate change and these studies are often limited by small sample size (Trapp and Hoogewind 2016; Molina et al. 2020; Carroll-Smith et al. 2020). Additionally, of the many studies that have examined the effects of climate change on severe storms, there has been a considerable focus on daytime spring events, as they are dominant in the United States (Kerr and Darkow 1996). Winter and nocturnal tornadic storms, however, can be extremely destructive and dangerous with high fatality rates (Ashley 2007; Ashley et al. 2008). Finally, previous research has focused on historical records from the past century (Doswell et al. 2012) and future climate simulations (Trapp et al. 2007, 2009; Diffenbaugh et al. 2013; Trapp and Hoogewind 2016; Hoogewind et al. 2017; Carroll-Smith et al. 2020), but not the pre-industrial climate. By examining the pre-industrial climate, we can develop a better understanding of how climate change from the past to the present has affected tornadic storm events.

The objective of this study is to advance understanding of anthropogenic influences on winter, nocturnal, and spring tornadic storms by examining the effects of climate change using high-resolution, convection-permitting WRF simulations. To address this objective, we focus on three tornadic storm events: the 31 December 2010 winter event near Ft. Leonard Wood, Missouri; the 3 March 2020 cool season nocturnal event near Nashville, Tennessee; and the 22 May 2011 spring event in Joplin, Missouri. Although we are only focusing on three events, the PGW method used in this study is well suited to allow insight into the impacts of climate change when

TABLE 1. List of tornado events, the time of the events as documented by the NOAA NCEI Storm Events Database, the time period of the model simulations, and the time period used for analysis.

Tornado event	Time of event	Simulation period	Analysis period
Ft. Leonard Wood, MO	0600–1600 UTC 31 Dec 2010	0000 UTC 27 Dec 2010–0000 UTC 3 Jan 2011	0600–1600 UTC 31 Dec 2010
Nashville, TN	0530–0700 UTC 3 Mar 2020	0000 UTC 28 Feb–0000 UTC 6 Mar 2020	0500–0800 UTC 3 Mar 2020
Joplin, MO	2230 UTC 22 May 2011	0000 UTC 18 May–0000 UTC 25 May 2011	2200 UTC 22 May–0000 UTC 23 May 2011

applied to even just a few cases, and has been used in a similar manner in prior studies. In the following sections, we address the question of how the favorability for tornadic storms during these three events could change if they occurred in the pre-industrial or future climates.

2. Methodology

a. Model

Simulations in this study were performed using the WRF Model (Skamarock et al. 2008) version 3.8.1. Previous studies have shown that dynamical downscaling is well suited for studying tornadic storms (Gensini and Mote 2015; Trapp and Hoogewind 2016; Hoogewind et al. 2017), as it allows for high-resolution, convection-permitting simulations that are not feasible with global climate models. Our choice of three tornadic storm events, however, was limited by the computing power required to run ensembles of high-resolution, convection-permitting WRF simulations of each event in different climate states.

Three tornadic storm hindcasts were simulated in the historical conditions in which they actually occurred. The historical timeframe for each event, as documented in the Storm Events Database (NOAA NCEI 2019), and the duration of the simulations are shown in Table 1. The 12-km-resolution North American Forecast System Analyses (NAM-ANL) was used to generate the initial and boundary conditions. Although these types of events are sensitive to the choice of initial and boundary conditions, NAM-ANL has previously been shown to produce reasonable tornadic storm simulations with WRF (Trapp and Hoogewind 2016). A five-member ensemble of each simulation was generated using the Stochastic Kinetic Energy Backscatter Scheme (SKEBS) (Shutts 2005; Berner et al. 2011). SKEBS uses random streamfunction perturbations to represent model uncertainty from unresolved scales and introduces perturbations at each time step. SKEBS has previously been used to generate WRF ensembles (Berner et al. 2011; Patricola and Wehner 2018; Lawson et al. 2020). We chose a five-member ensemble for each climate state of each event because it was sufficient to identify climate change signals through any noise from model internal variability.

Model output was generated every hour with 35 vertical levels and a convection-permitting grid spacing of 3 km, which sufficiently reproduces mesoconvective circulations (Weisman et al. 1997; Potvin and Flora 2015). The simulation domains are shown in Fig. 1, where the red boxes show the regions used in the analysis. Parameterization schemes used in all simulations

include the Rapid Radiative Transfer Model for Global Climate Models (Iacono et al. 2008) shortwave and longwave schemes, the Morrison double-moment microphysics scheme (Morrison et al. 2009), the Noah land surface model scheme (Chen and Dudhia 2001), and the Mellor–Yamada–Janjić planetary boundary layer scheme (Janjić 1994). Although the choice of parameterizations introduces an element of uncertainty, previous research has shown that these parameterization schemes are effective for hindcasts of tornadic storms with WRF (Trapp and Hoogewind 2016). While we acknowledge the potential sensitivity of our simulations to the choice of parameterization schemes, exploring this sensitivity was beyond the scope of this study.

b. Pseudo-global warming experiments

To examine the effects of climate change, ensembles of simulations were performed for the winter, nocturnal, and spring events as if they were to occur in a pre-industrial climate, and in mid- and late-twenty-first-century climates under the Shared Socioeconomic Pathways (SSPs) 585 (Riahi et al. 2017) scenario. To perform these simulations, we use the PGW method (Schär et al. 1996; Lackmann 2015; Patricola and Wehner 2018), where the initial and lateral boundary conditions from the historical simulations were adjusted by a climate change difference, or delta, that takes into account the thermodynamic component of anthropogenic climate change. By using the PGW method, we are assuming that similar synoptic conditions that produced the tornadic storm events in the historical time period could happen in the pre-industrial and future climate. This is a reasonable assumption, however, because we expect that winter, nocturnal, and spring tornadic storm events will still occur in the different climate states. The PGW method, therefore, allows us to examine how the tornadic storm events would change under different background climate states, assuming similar synoptic conditions. For the pre-industrial and future climate simulations, the variables adjusted in the initial and boundary conditions include temperature, relative humidity, geopotential height, sea-level and surface pressure, sea surface temperature, surface temperature, and soil moisture and temperature. Additionally, we modified the WRF radiation code to account for different greenhouse gas concentrations of CO₂, CH₄, N₂O, CFC-11, CFC-12, and CCl₄ in the pre-industrial and future climate simulations (Meinshausen and Vogel 2016).

The pre-industrial, mid-twenty-first-century, and late-twenty-first-century PGW deltas were calculated from the Coupled

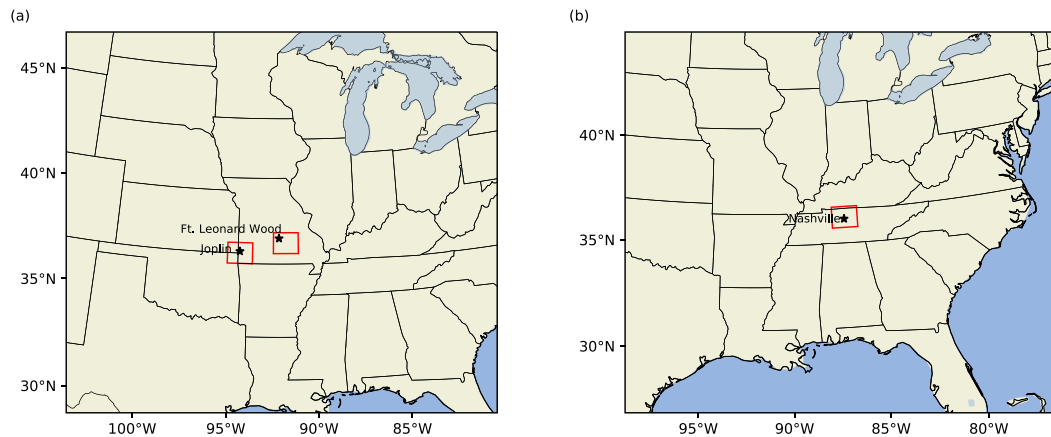


FIG. 1. WRF domains for the (a) Ft. Leonard Wood and Joplin, Missouri (MO) and the (b) Nashville, Tennessee (TN) tornado events. Red boxes show the analysis regions for the three tornado events.

Model Intercomparison Project phase 6 (CMIP6) Community Earth System Model (CESM2) (Danabasoglu 2019) data by subtracting the CESM2 1950–2014 averaged historical simulation from 1) the averaged pre-industrial control (piControl) simulation (Eyring et al. 2016), 2) the 2040–60 averaged SSP585 simulation, and 3) the 2080–2100 averaged SSP585 simulation. The length of the historical timeframe was chosen to capture the historical climate and to smooth out any multidecadal variability. The piControl simulation represents a stable quasi-equilibrium climate state under 1850 conditions (Eyring et al. 2016) and the SSP585 simulation incorporates future emissions and land use changes (O'Neill et al. 2016). Deltas were calculated for each month of the corresponding event and were added to the corresponding initial and boundary conditions (i.e., the delta for May was used for the Joplin event). Each CESM2 simulation consists of one ensemble member with 1° resolution. By using one model to calculate the deltas, we are only considering the climate sensitivity of the CESM2 model. The uncertainty from the range of climate sensitivities was not accounted for in this study due to the limitation of computing power. However, comparing the climate sensitivity of CESM2 to other CMIP6 models indicates that CESM2 is on the higher end of warming, so it is possible that the changes simulated in this study may happen at a slower timeframe than seen here

(Dong et al. 2020; Nijse et al. 2020). If the changes simulated in this study do indeed happen at a slower timeframe, the mid-twenty-first-century climate scenario in this study could potentially represent the climate at the end of the twenty-first century.

Figure 2 shows March surface temperature differences over the contiguous United States to illustrate the CESM2 response to climate change. Although much of the globe was cooler during the pre-industrial period compared with the historical, pre-industrial surface temperatures were warmer over the eastern half of the United States (Fig. 2a). This feature is commonly referred to as the “warming hole,” where there was a cooling trend of annual-mean surface temperatures over the eastern half of the United States during the second half of the twentieth century (Pan et al. 2004; Kunkel et al. 2006). Although the cause of the warming hole is not definitively known, it has been attributed to anthropogenic aerosols in the twentieth century (Leibensperger et al. 2012). As expected, warmer surface temperatures are seen over the United States in both the middle and late twenty-first century compared with the historical (Figs. 2b,c), a consequence of anthropogenic climate change in the SSP585 scenario. To show the effect of the deltas, Figs. 3–5 show the ensemble-averaged 2-m temperature in the historical period (panel a of each figure), and temperature difference in the pre-industrial, mid-century, and

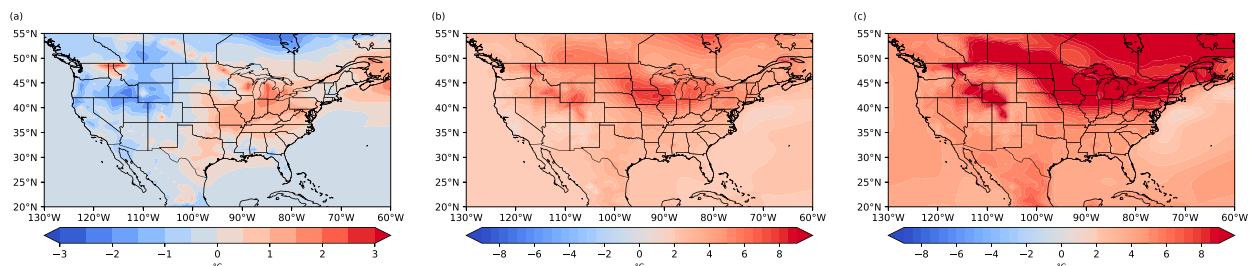


FIG. 2. CMIP6 CESM2 March surface temperature differences over the contiguous United States: (a) pre-industrial – historical, (b) mid-century – historical, and (c) late-century – historical simulations. The pre-industrial is the average of the piControl simulation; the historical is the 1950–2014 average of the historical simulation; the mid-century is the 2040–60 average of the SSP585 simulation; and the late-century period is the 2080–2100 average of the SSP585 simulation. Note the different contour scales.

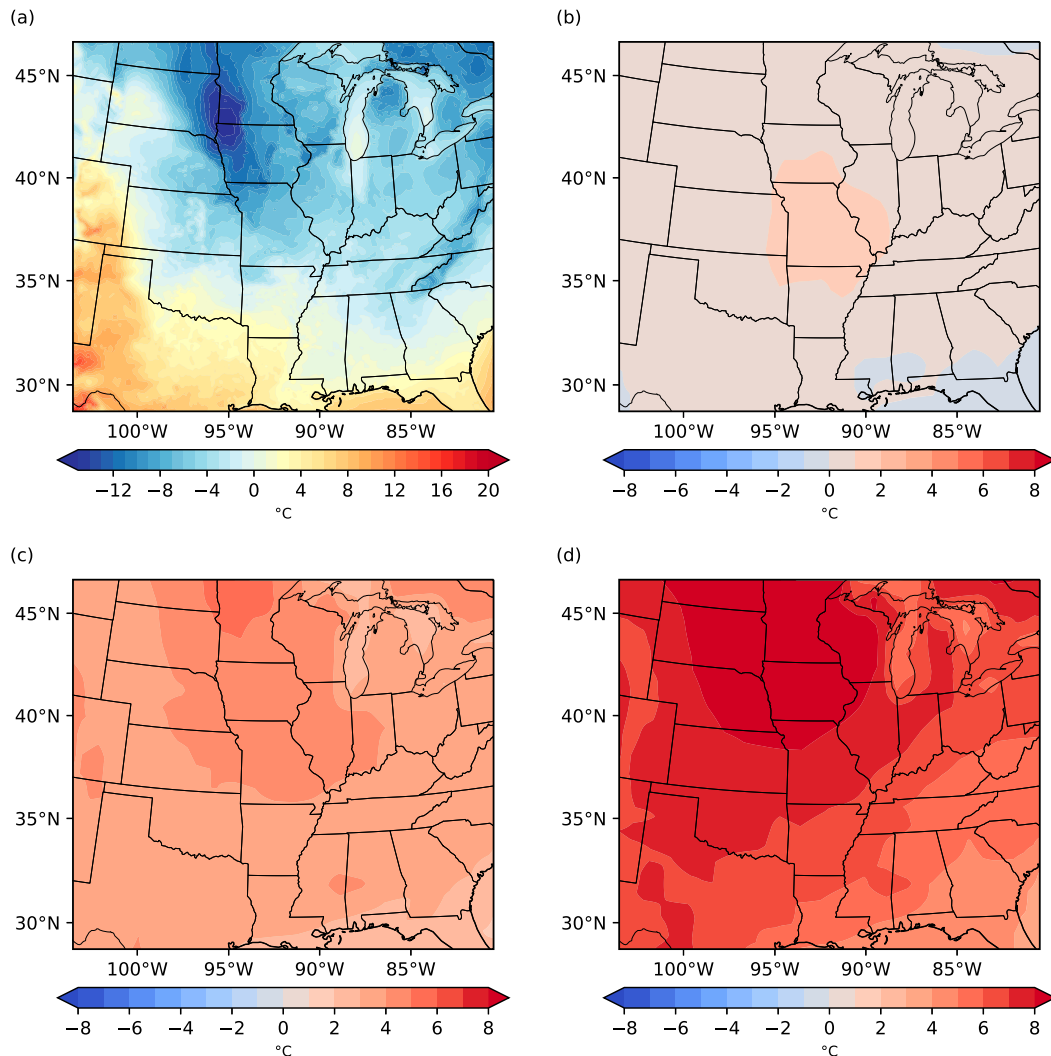


FIG. 3. Ensemble-averaged 2-m (a) temperature ($^{\circ}\text{C}$) for the historical simulation, and temperature differences for the (b) pre-industrial minus historical, (c) mid-century minus historical, and (d) late-century minus historical simulations at 0000 UTC 27 Dec 2010 for the winter tornado event near Ft. Leonard Wood, MO.

late-century periods minus the historical period (panels b–d, respectively) at the initial times of the winter, nocturnal, and spring simulations. In all three events, there is 1° – 2° of warming in the pre-industrial when compared with the historical, consistent with the warming hole seen in the global climate model data. Figures 3–5 also show significant warming in the mid- and late-century periods when compared with the historical, which is consistent with the SSP585 scenario.

c. Three tornadic storm events

For the winter and nocturnal events, the tornadic storms developed ahead of approaching cold fronts. Before the winter event, an upper-level trough and surface low moved eastward across the Great Plains and a cold front advanced from the Dakotas toward Missouri. Multiple tornadic storms developed on 31 December 2010, including an EF-1 tornado in Christian County at \sim 0600 UTC and an EF-3 tornado in Pulaski County

at \sim 1530 UTC (NCDC 2010). Similarly, before the nocturnal event, a trough deepened over the upper Midwest, and a surface low and cold front advanced toward Tennessee. Additionally, a warm front was oriented in the north–south direction over Tennessee. On 3 March 2020, multiple tornadic storms developed from the same parent supercell that began in West Tennessee and traversed to the east, including an EF-3 tornado in Nashville at \sim 0630 UTC (NOAA NCEI 2019).

In contrast to the winter and nocturnal events, the spring event was preceded by a slow evolution of surface and upper air features (Davies 2017), including an upper-level trough that moved slowly eastward across the upper Great Plains. This slow progression allowed a low-level jet east of the trough to transport warm, moist air from the Gulf of Mexico to southern Missouri. On the day of the event, the dryline was located over southeast Kansas and a cold front associated with a surface low over Minnesota extended down to a secondary low over

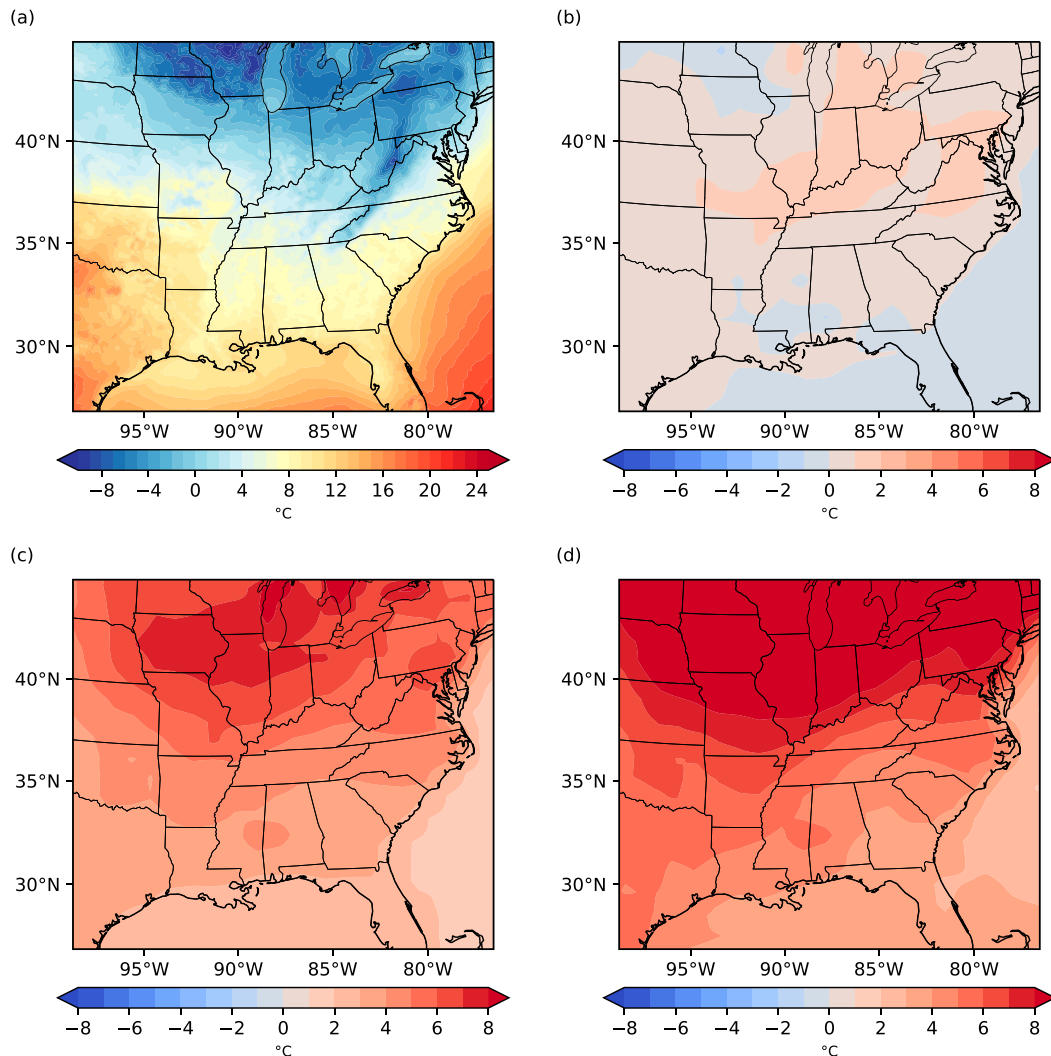


FIG. 4. As in Fig. 3, but at 0000 UTC 28 Feb 2020 for the nocturnal tornado event near Nashville, TN.

southeast Kansas where it became a stationary front. These conditions created an environment of high CAPE and SRH, leading to the devastating EF-5 tornado in Joplin, Missouri, at ~2230 UTC 22 May 2011 (NCDC 2011).

To verify the development of supercells for the three events in the WRF simulations, we used instantaneous hourly 2–5-km updraft helicity (UH) and maximum simulated reflectivity in the column for each grid point. UH embodies the convective updraft and storm-generated vertical rotation of supercells (Kain et al. 2008) and has been used as a surrogate for supercells (Sobash et al. 2016; Trapp and Hoogewind 2016; Gallo et al. 2016; Molina et al. 2020; Carroll-Smith et al. 2020). For climate models with 3–4-km resolution, UH values of 40–150 m² s⁻² have previously been used to indicate supercell existence at model grid points (Trapp et al. 2011; Robinson et al. 2013). Although it is common to use maximum hourly UH, here we detect large UH values that indicate that our simulations are correctly producing strongly rotating storms similar to what was observed in the three cases. The purpose of

examining the UH and the maximum simulated reflectivity is to establish that supercells develop at some point within the time period and in the region of the storm event. As with weather forecasts, we would not expect the hindcast simulations to reproduce the exact events, particularly location and timing, from the historical record.

Figures 6–8 show the UH for the pre-industrial (panels a and e), historical (panels b and f), mid-century (panels c and g), and late-century simulations (panels d and h) for the winter, nocturnal, and spring events, respectively. Figures 6–8 use the spatial domains shown as red boxes in Fig. 1, which are centered around the tornadic storm events, and the analysis time periods based on the timing of the tornadic storm events (see Table 1). The UH and maximum simulated reflectivity are also shown for each ensemble member and at individual times during the winter, nocturnal, and spring storm events in supplemental Figs. 1, 3, and 5 (see the online supplemental material), respectively. Although we would not expect the hindcast simulations to exactly reproduce the historical events, the

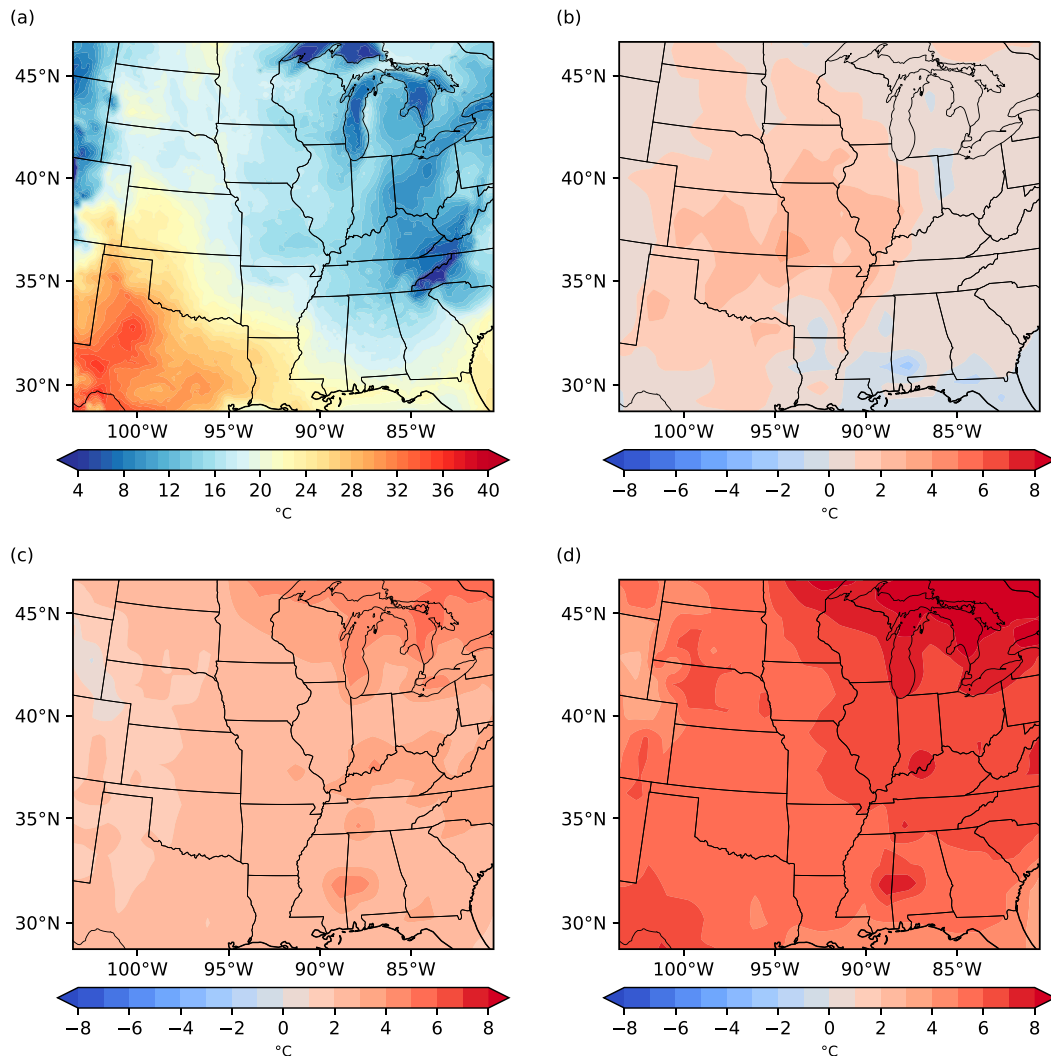


FIG. 5. As in Fig. 3, but at 0000 UTC 18 May 2011 for the spring tornado event in Joplin, MO.

simulated events should be reasonably close in space and time. Here we define reasonably close in space as within ~ 50 km of the actual event, which is roughly half the average displacement error found for convective initiation (Duda and Gallus 2013) and mesoscale convective system centroids (Yan and Gallus 2016; Geerts et al. 2017) in short-range model forecasts. We define reasonably close in time as within ~ 3 h of the actual event, which has previously been used as an acceptable time difference in comparing models to observations (Done et al. 2004) and as the grace period for a morphology skill score application (Snively and Gallus 2014).

In Figs. 6a–d, the maximum ensemble member accumulated UH shows regions of large UH in all climate scenarios of the winter event, indicative of rotating storms. The track of the EF3 tornado in Pulaski County is shown in the historical panels (Figs. 6b,f) and is reasonably close to the simulated storm activity. To visualize the spread of the ensemble members, Figs. 6e–h show “paintball” plots, where each ensemble member exceeding $40 \text{ m}^2 \text{ s}^{-2}$ is shown as a different color. The paintball

plots indicate that in each of the climate scenarios for the winter event, multiple ensemble members are capturing storm activity. Additionally, the UH and maximum simulated reflectivity in supplemental Fig. 1 demonstrate that multiple ensemble members are capturing rotating storm activity within a reasonable time and distance from the actual historical winter event. Supplemental Fig. 1 also demonstrates that multiple ensemble members were found to capture the quasi-linear convective system structure seen in the observations (see supplemental Fig. 2).

In the nocturnal event, Figs. 7a–d show large UH values indicative of rotating storms and Figs. 7e–h show that multiple ensemble members are capturing storm activity in each of the climate scenarios. The track of the EF3 tornado that affected Nashville is shown in the historical panels (Figs. 7b,f) and is close to simulated storm activity. Similar to supplemental Fig. 1, the UH and maximum simulated reflectivity in supplemental Fig. 3 demonstrate that multiple ensemble members are capturing rotating storm activity within a reasonable

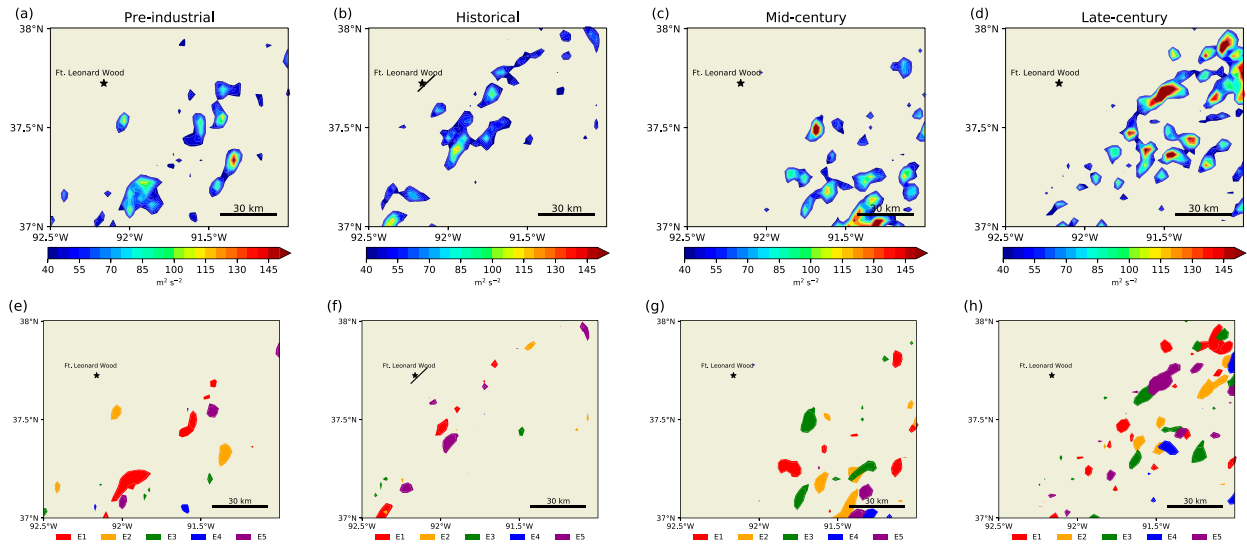


FIG. 6. Updraft helicity ($\text{m}^2 \text{s}^{-2}$) accumulated over the period 0600–1600 UTC 31 Dec 2010 for the (a),(e) pre-industrial, (b),(f) historical, (c),(g) mid-century, and (d),(h) late-century simulations of the event near Ft. Leonard Wood, MO. In (a)–(d), the ensemble maximum updraft helicity is accumulated over the time period. In (e)–(h), each ensemble is shown as a different color and contours are shown for values greater than $40 \text{ m}^2 \text{ s}^{-2}$. Black lines in the historical panels show the EF3 tornado track from the NCEI Storm Events Database.

time and distance from the actual historical nocturnal event. Supplemental Fig. 3 also demonstrates that multiple ensemble members capture the east–west structure of the storms in an event like the nocturnal tornadic storm, as seen in observations (see supplemental Fig. 4).

In the spring event, Figs. 8a–d also show large UH values and Figs. 8e–h show that rotating storms are simulated in multiple ensembles across the climate scenarios. The track of the Joplin EF5 tornado is shown in the historical panels (Figs. 8b,f) and there is clear simulated storm activity in the vicinity of the track. As with the winter and nocturnal events,

the UH and maximum simulated reflectivity in supplemental Fig. 5 demonstrate that multiple ensemble members are capturing rotating storm activity within a reasonable time and distance from the actual historical spring event. Supplemental Fig. 5 also shows that multiple ensemble members are capturing the correct type of storms, scattered cells, of an event like the spring tornadic storm (see supplemental Fig. 6).

We next examine the maximum simulated reflectivity. Previous studies have used simulated reflectivity values greater than 30–40 dBZ to identify convective storms (Trapp and Hoogewind 2016; Carroll-Smith et al. 2020). Figure 9 shows the

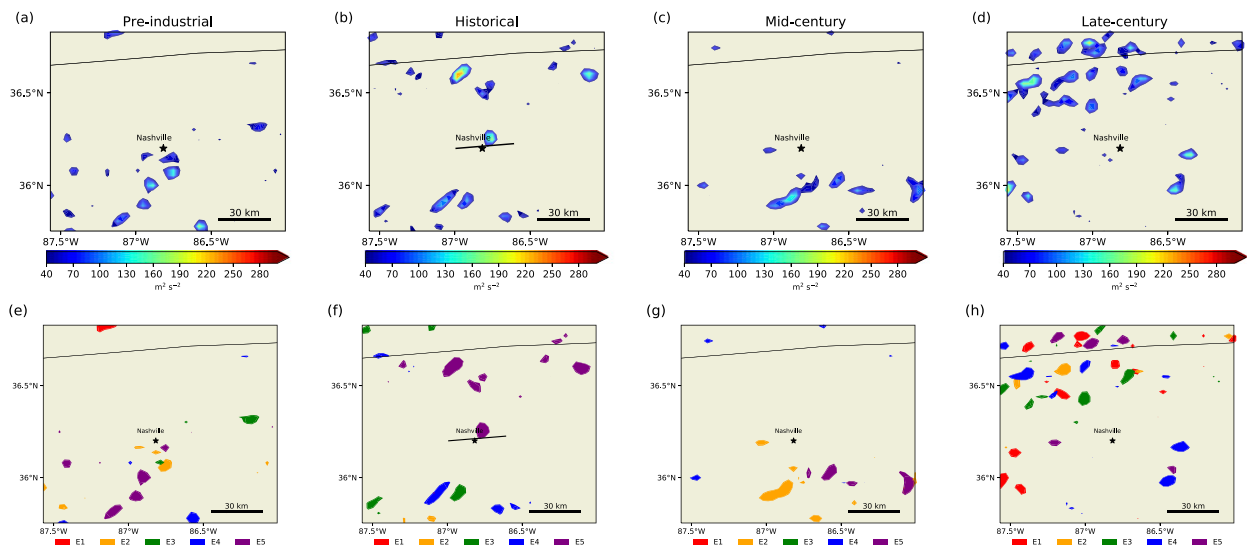


FIG. 7. As in Fig. 6, but updraft helicity values are accumulated over the period 0500–0800 UTC 3 Mar 2020 for the tornado event near Nashville, TN. Black lines in the historical panels show the EF3 tornado track from the NCEI Storm Events Database.

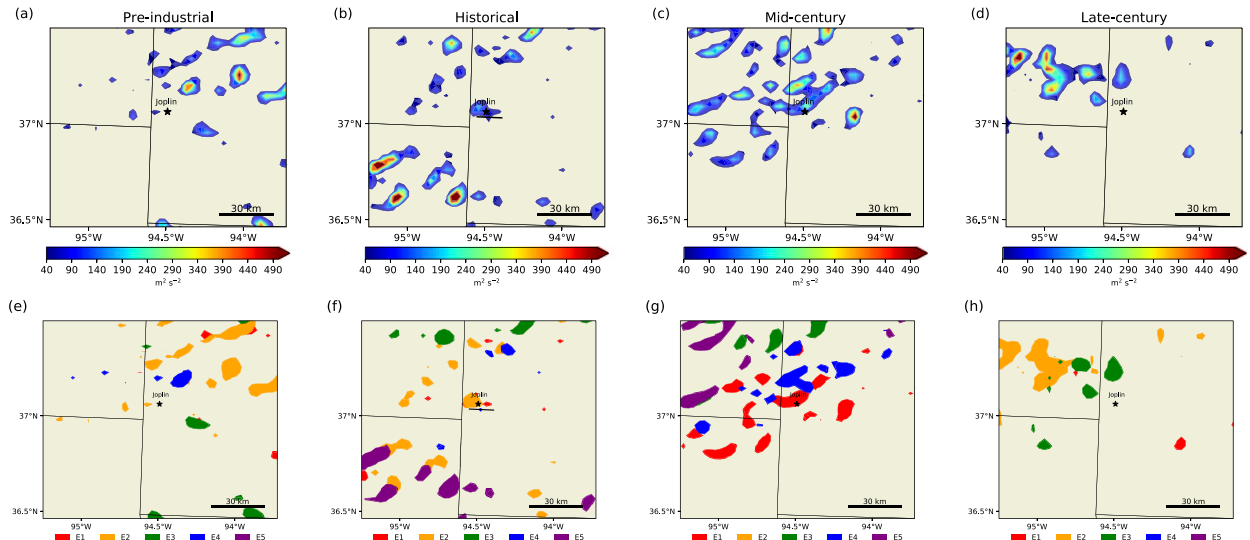


FIG. 8. As in Fig. 6, but updraft helicity values are accumulated over the period 2200 UTC 22 May–0000 UTC 23 May 2011 for the tornado event in Joplin, MO. Black lines in the historical panels show the EF5 tornado track from the NCEI Storm Events Database.

count across all five ensembles and the analysis time period (see Table 1) where the historical maximum simulated reflectivity is greater than 40 dBZ in the winter (Fig. 9a), nocturnal (Fig. 9b), and spring events (Fig. 9c). In all three events, Fig. 9 indicates that across all ensembles the historical maximum simulated reflectivity exceeds 40 dBZ in the region and during the time of the tornadic storms. The UH shown in Figs. 6–8 and supplemental Figs. 1, 3, and 5 and the maximum simulated reflectivity exceedances shown in Fig. 9 together indicate convective storms. We are therefore confident that supercells exist in the WRF simulations of the three tornadic storm events.

3. Anthropogenic changes in tornadic storm events

a. Changes in simulated storms

To examine how climate change has affected the three tornadic storms events, we rely on the UH and maximum simulated reflectivity because the 3-km WRF simulations do not

explicitly resolve tornadoes. As in Carroll-Smith et al. (2020), storms are identified in the simulations using grid point-based exceedances of UH and maximum simulated reflectivity. We chose thresholds of $40 \text{ m}^2 \text{ s}^{-2}$ and 40 dBZ for the UH and maximum simulated reflectivity, respectively, based on previous research (Trapp et al. 2011; Robinson et al. 2013; Trapp and Hoogewind 2016; Carroll-Smith et al. 2020). Grid point exceedances were calculated where $\text{UH} > 40 \text{ m}^2 \text{ s}^{-2}$ and the maximum simulated reflectivity $> 40 \text{ dBZ}$ from the analysis domains (see Fig. 1), across the analysis time periods (see Table 1) and for all ensemble members. We include all ensemble members because the individual members show storm activity in multiple climate scenarios (Figs. 6–8) and using all ensembles accounts for the high amount of internal atmospheric variability.

Figure 10 shows the fractional change of grid point exceedances (Fig. 10a), maximum UH (Fig. 10b), and maximum vertical velocity (w) (Fig. 10c) from the past and future climates relative to the historical in the winter (blue circles),

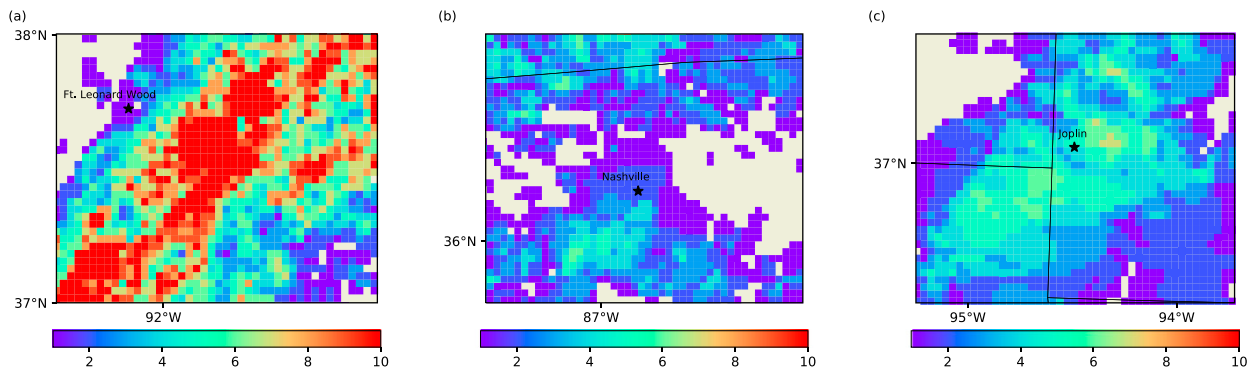


FIG. 9. Count per grid cell over all five ensemble members and the analysis time periods in Table 1 of maximum simulated reflectivity greater than 40 dBZ in the (a) Ft. Leonard Wood (winter), (b) Nashville (nocturnal), and (c) Joplin (spring) historical simulations.

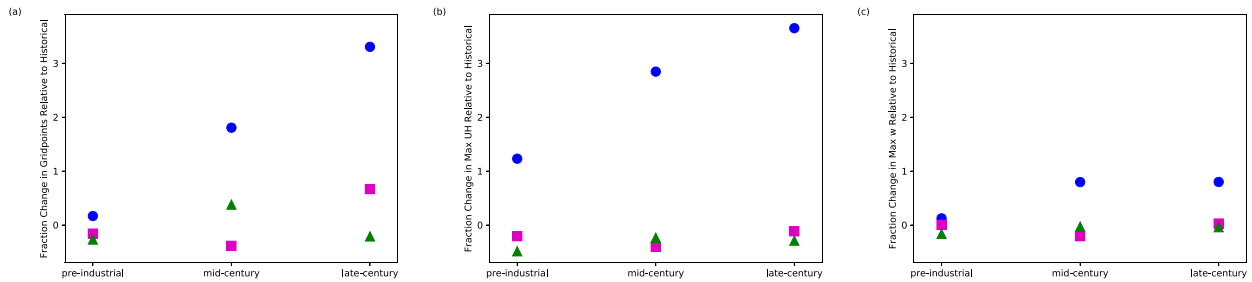


FIG. 10. Fractional change relative to the historical in (a) grid points with updraft helicity (UH) greater than $40 \text{ m}^2 \text{ s}^{-2}$ and maximum simulated reflective greater than 40 dBZ, (b) maximum UH, and (c) maximum vertical velocity (w) for the Ft. Leonard Wood winter event (blue circles), the Nashville nocturnal event (purple squares), and the Joplin spring event (green triangles). For (a), grid point exceedances are calculated from all ensembles, from the analysis domain shown in Fig. 1, and the analysis time period listed in Table 1. For (b) and (c), the maximum UH and w are calculated from the grid points where $\text{UH} > 40 \text{ m}^2 \text{ s}^{-2}$ and the maximum simulated reflectivity $> 40 \text{ dBZ}$.

nocturnal (magenta squares), and spring (green triangles) events. The grid point exceedances were calculated as described in the previous paragraph and the maximum UH and w were calculated from the grid point exceedance points. For the winter event, there is a clear increase in maximum UH and w (Figs. 10b,c) and grid point exceedances (Fig. 10a) in the pre-industrial, mid-century, and late-century periods when compared to the historical. The past and future simulations of the winter event therefore have stronger rotating updrafts (Figs. 10b,c) and an increase in storm activity (Fig. 10a), which we define as an increase in grid points that exceed $\text{UH} > 40 \text{ m}^2 \text{ s}^{-2}$ and maximum simulated reflectivity $> 40 \text{ dBZ}$. For the nocturnal event, the pre-industrial and mid-century have a decrease in storm activity and weaker rotating updrafts compared to the historical. In contrast, the late-century period has an increase in storm activity but slightly weaker rotating updrafts. For the spring event, only the mid-century has an increase in storm activity compared to the historical, and the past and future climates all indicate weaker rotating updrafts. For all three events, increased storm activity could be due to an increase in the number of individual storms, a larger extent of storms, and/or a change in storm mode. Identifying the exact cause for the changes in storm activity is beyond the scope of this study. It is, however, noteworthy that only the winter event shows an increase in storm activity and stronger rotating updrafts in the future climate.

To examine updraft intensity, Fig. 11 shows the actual and parcel theory maximum w for the pre-industrial (green), historical (blue), mid-century (orange), and late-century (red) climate scenarios in the winter (circles), nocturnal (squares), and spring (triangles) events. The maximum w is calculated from the grid points where $\text{UH} > 40 \text{ m}^2 \text{ s}^{-2}$ and the maximum simulated reflectivity $> 40 \text{ dBZ}$, and the parcel theory maximum w is calculated from the analysis domain and time-averaged surface-based CAPE. We chose to use the domain averaged CAPE to calculate the parcel theory maximum w based on previous research (Trapp and Hoogewind 2016; Peters et al. 2020). In all but two events and climate scenarios, the parcel theory maximum w is greater than the actual maximum w , which is not surprising given that parcel theory provides an upper bound on maximum w (Crook 1996). Similar to Trapp and Hoogewind (2016), the largest difference between

the parcel theory w and the actual maximum w occurs in the late-century period in all three events. This difference suggests less realization of the potential buoyancy, which could possibly be due to the entrainment of dry air or an increase in precipitation loading (Trapp and Hoogewind 2016). The results from Fig. 11, however, do not necessarily equate to less storm activity. For example, Fig. 10a shows a late-century increase in storm activity in the winter and nocturnal events, while Fig. 11 shows a discrepancy between the parcel theory maximum w and the actual maximum w . Despite less realization of the potential buoyancy, the overall conditions in the late-century climate of the winter and nocturnal events were favorable for increased storm activity.

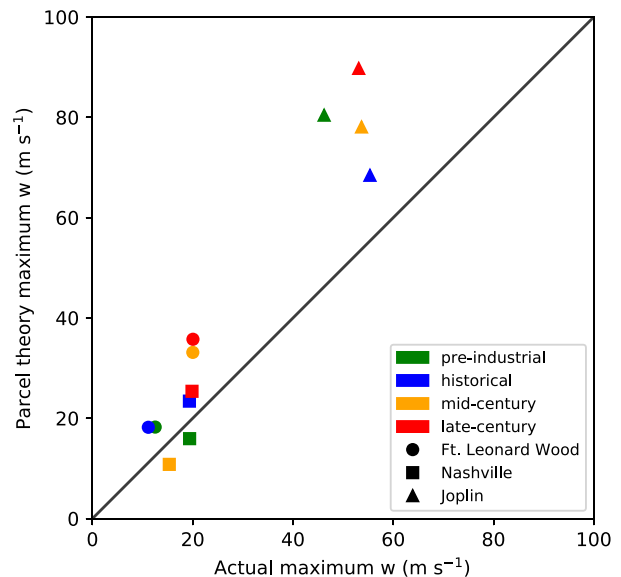


FIG. 11. Scatterplot of peak values of vertical velocity (m s^{-1}) vs peak values predicted by parcel theory (m s^{-1}) using the average surface-based CAPE. Points are shown for the Ft. Leonard Wood winter event (circles), the Nashville nocturnal event (squares), and the Joplin spring event (triangles) and for the pre-industrial (green), historical (blue), mid-century (orange), and late-century (red) climate scenarios.

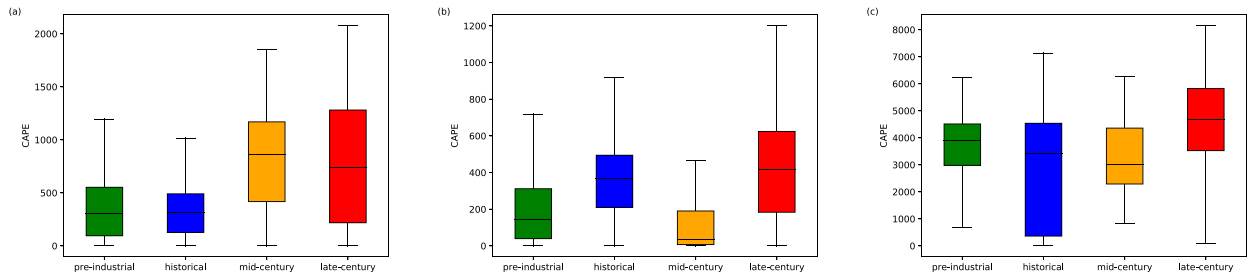


FIG. 12. Boxplots of the surface-based CAPE (J kg^{-1}) from the pre-industrial (green), historical (blue), mid-century (orange), and late-century (red) simulations in the (a) Ft. Leonard Wood (winter), (b) Nashville (nocturnal), and (c) Joplin (spring) events. The boxplots only include points where the most unstable CAPE is not zero and the maximum simulated reflectivity is less than 20 dBZ across all five ensembles, from the analysis domain shown in Fig. 1, and the analysis time period listed in Table 1. Each box shows the interquartile range (IQR) from the first quartile (Q1) to the third quartile (Q3), where the horizontal line represents the median. The whiskers of the box extend from $Q1 + 1.5 \times \text{IQR}$ to $Q3 - 1.5 \times \text{IQR}$. Note the different scales used.

b. Changes in environment

To understand how thermodynamic and dynamic factors influence the three tornadic storm events, we next examine the surface-based CAPE, the 2-m temperature, the 0–1-km SRH, and the magnitude of the surface-based CIN. Figures 12–15 show boxplots of the CAPE, temperature, SRH, and CIN in the pre-industrial (green), historical (blue), mid-century (orange), and late-century (red) for the winter, nocturnal, and spring events (panels a, b, and c, respectively, in each figure). The values used in each boxplot are from where the most unstable CAPE is not zero and the maximum simulated reflectivity is less than 20 dBZ across all ensembles, the analysis domains in Fig. 1, and the analysis time periods in Table 1. This choice of values avoids any convective contamination to our environmental analysis (Thompson et al. 2003; Mauri and Gallus 2021) and avoids portions of the domain that are likely within a different airmass and not playing a role in thunderstorm development or sustenance.

We begin with an analysis of the CAPE (Fig. 12). In the winter event (Fig. 12a), the CAPE distributions in the pre-industrial and historical climates are similar, with median values near 300 J kg^{-1} . In contrast, the CAPE in the future climate has greater variability and is considerably larger than the historical, with mid- and late-century median values of 863 and 742 J kg^{-1} , respectively. In the nocturnal event (Fig. 12b), the CAPE in the pre-industrial climate is notably less than in the historical, with the median CAPE in the historical more than

twice that in the pre-industrial. The CAPE in the mid-century climate is significantly less than the historical and the majority of the distribution does not exceed 200 J kg^{-1} . The late-century climate, however, has greater variability and higher values of CAPE than the historical period, with the 75th percentile extending to 624 J kg^{-1} . In the spring event (Fig. 12c), the pre-industrial distribution has less variability than in the historical, although the median is shifted to higher CAPE: 3912 and 3421 J kg^{-1} in the pre-industrial and historical, respectively. The mid-century CAPE distribution has less variability and is shifted to lower values of CAPE than in the historical period. In contrast, the late-century simulation has large variability and extends to include extremely high values of CAPE, with a median value of 4678 J kg^{-1} . Both the winter and nocturnal events have lower CAPE environments, which is typical of winter and nocturnal events (Kis and Straka 2010; Sherburn and Parker 2014), whereas the historical CAPE is considerably higher in the spring event, consistent with observational data from the University of Wyoming (University of Wyoming 2020). In all three events, the late-century CAPE has large variability and the highest extreme values, in agreement with previous research (Del Genio et al. 2007; Trapp et al. 2009; Diffenbaugh et al. 2013; Trapp and Hoogewind 2016).

Next we analyze the temperature (Fig. 13). In the winter event (Fig. 13a), the pre-industrial and historical temperature distributions are similar, although the historical climate has less variability and is slightly warmer. The future climate,

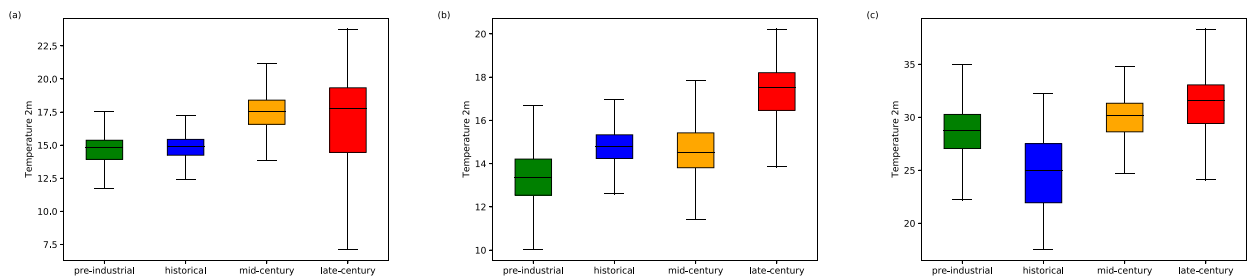


FIG. 13. As in Fig. 12, but the pre-industrial (green), historical (blue), mid-century (orange), and late-century (red) 2-m temperature ($^{\circ}\text{C}$) for the (a) Ft. Leonard Wood (winter), (b) Nashville (nocturnal), and (c) Joplin (spring) events. Note the different scales used.

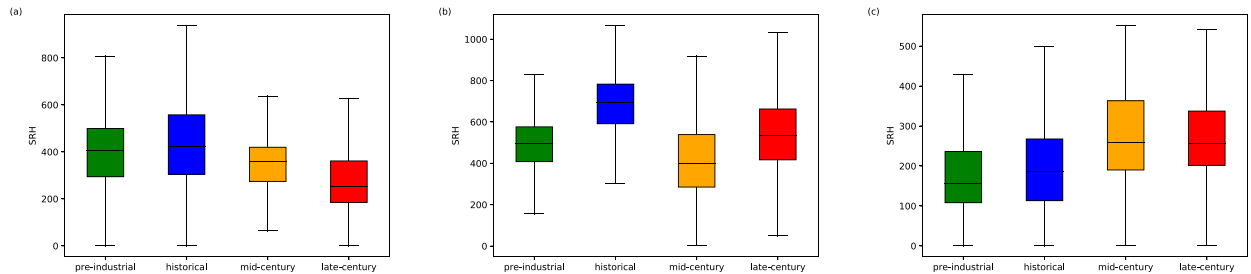


FIG. 14. As in Fig. 12, but the pre-industrial (green), historical (blue), mid-century (orange), and late-century (red) 0–1-km SRH ($\text{m}^2 \text{s}^{-2}$) for the (a) Ft. Leonard Wood (winter), (b) Nashville (nocturnal), and (c) Joplin (spring) events. Note the different scales used.

however, is significantly warmer than in the historical, with a $\sim 3^\circ\text{C}$ increase in the median temperature. The 2-m temperature and precipitable water for each climate scenario of the winter event are shown in supplemental Figs. 7 and 8, respectively. The future increase in temperature can be clearly seen in supplemental Fig. 7 and a corresponding increase in precipitable water is apparent in supplemental Fig. 8. In the nocturnal event (Fig. 13b), the pre-industrial climate is cooler and has larger variability than the historical. The historical and mid-century temperature distributions are similar, although the mid-century is slightly cooler. In contrast, the temperature in the late-century climate is warmer than the historical, with a $\sim 3^\circ\text{C}$ increase in the median temperature. The 2-m temperature and precipitable water, shown in supplemental Figs. 9 and 10, respectively, also show warming as well as an increase in atmospheric water vapor in the future climate. In the spring event (Fig. 13c), the temperature distribution in the pre-industrial is warmer than in the historical, likely an artifact of the warming hole discussed in section 2. The temperature distributions in the future climate show warming compared to the historical, with an $\sim 5^\circ\text{--}6^\circ\text{C}$ increase in the median temperatures. As in the winter and nocturnal events, the 2-m temperature and precipitable water, shown in supplemental Figs. 11 and 12, respectively, also show a future increase in temperature and atmospheric water vapor. In all three storm events, the late-century climate has both the highest temperature, precipitable water and CAPE values, which is in agreement with previous research (Diffenbaugh et al. 2013; Seeley and Romps 2014).

Next we analyze SRH (Fig. 14). In the winter event (Fig. 14a), the SRH in the pre-industrial climate is similar to

the historical, with median values of 404 and $422 \text{ m}^2 \text{ s}^{-2}$, respectively. In contrast, the SRH in the future climate is smaller than in the historical, with mid- and late-century median values of 360 and $251 \text{ m}^2 \text{ s}^{-2}$, respectively. In the nocturnal event (Fig. 14b), the SRH in the pre-industrial climate is less than the historical, with median values of 495 and $692 \text{ m}^2 \text{ s}^{-2}$, respectively. In the future climate, the SRH is also less than in the historical, with mid- and late-century median values of 399 and $532 \text{ m}^2 \text{ s}^{-2}$, respectively. In the spring event (Fig. 14c), the pre-industrial distribution of SRH is similar to the historical, although the historical has greater variability and higher maximum values. In contrast to the winter and nocturnal events, SRH is larger in the spring future climate than in the historical, with a median SRH of $186 \text{ m}^2 \text{ s}^{-2}$ in the historical and 258 and $256 \text{ m}^2 \text{ s}^{-2}$ in the mid- and late-century periods, respectively. This future increase in SRH is due to a strengthening of the 0–1-km flow, with the greatest strengthening at 1 km, which is in agreement with the future increase in 0–1-km shear found by Diffenbaugh et al. (2013). The strengthened 0–1-km flow stems from an increased surface pressure gradient that is associated with a stronger surface low and deeper 500-hPa trough in the future climate. A comparison of the three storm events indicates that the winter and nocturnal events have higher SRH environments than the spring event, but only the spring event experiences a future increase in SRH. Elevated SRH creates an environment that is more likely to be associated with potentially violent tornadoes, whereas a reduction in SRH could indicate weaker tornado development, or even a change in storm mode (Thompson et al. 2003; Coffey et al. 2019, 2020).

Finally, we analyze CIN (Fig. 15). In the winter event (Fig. 15a), the pre-industrial CIN distribution has larger

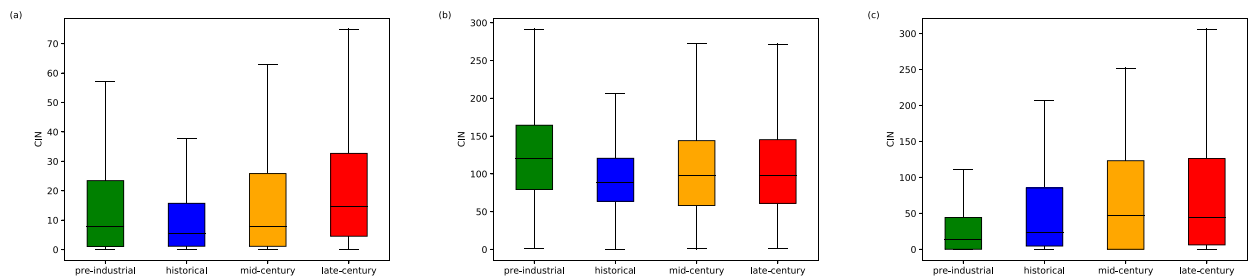


FIG. 15. As in Fig. 12, but the pre-industrial (green), historical (blue), mid-century (orange), and late-century (red) surface-based CIN (J kg^{-1}) for the (a) Ft. Leonard Wood (winter), (b) Nashville (nocturnal), and (c) Joplin (spring) events. Note the different scales used.

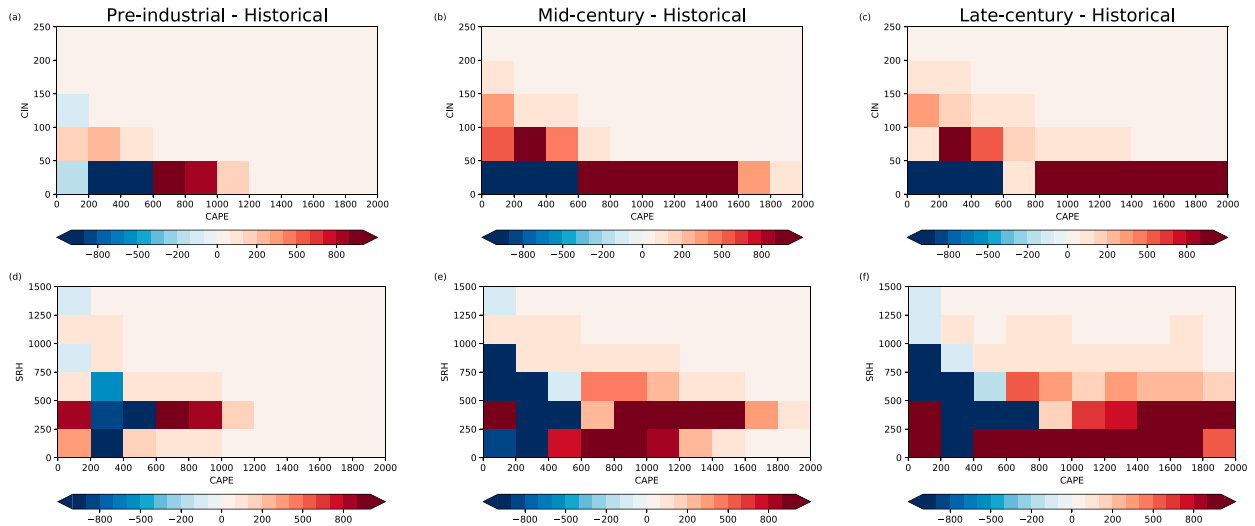


FIG. 16. Phase space differences of surface-based CAPE (J kg^{-1}) vs (a)–(c) surface-based CIN (J kg^{-1}) and (d)–(f) 0–1-km SRH ($\text{m}^2 \text{s}^{-2}$). Each shaded box represents differences in the number of grid points within the bounds of the box for the (a),(d) pre-industrial minus historical, (b),(e) mid-century minus historical, and (c),(f) late-century minus historical for the winter event near Ft. Leonard Wood, MO. Grid points are only used in the difference calculations if the most unstable CAPE is not zero and the maximum simulated reflectivity is less than 20 dBZ across all five ensembles, from the analysis domain shown in Fig. 1, and the analysis time period listed in Table 1.

extreme values and greater variability than in the historical, although both climate scenarios have median CIN values near 6 J kg^{-1} . The CIN in the future climate is larger and the distributions have greater variability than in the historical. The median values, however, are still relatively low: 8 and 14 J kg^{-1} in the mid- and late-century periods, respectively. In the nocturnal event (Fig. 15b), the CIN is larger and has greater variability in the pre-industrial than in the historical, with median values of 120 and 88 J kg^{-1} , respectively. The CIN distributions in the future climate have greater variability and larger extreme values than in the historical, but the median values are close to the historical: 97 J kg^{-1} in both the mid- and late-century periods. In the spring event (Fig. 15c), the CIN is lower in the pre-industrial than in the historical climate, with median values of 13 and 23 J kg^{-1} , respectively. The CIN distribution in the future climate is shifted to larger values and has greater variability than in the historical, with median values of 45 J kg^{-1} in both the mid- and late-century periods. Overall, the magnitude of CIN is higher in the nocturnal and spring events than in the winter event, which may serve to counteract CAPE and prevent robust storms from developing (Trapp and Hoogewind 2016; Rasmussen et al. 2017; Hoogewind et al. 2017; Taszarek et al. 2020). In contrast, the future low magnitude of CIN and increase in CAPE in the winter event suggests a potential for more robust storms to develop, in agreement with Fig. 10.

c. Overall changes in tornadic storm favorability

The above environmental analysis provides information on individual thermodynamic and/or dynamic factors that contribute to the climate-related changes in the three tornadic storm events. However, favorable environments for tornadic

storms involve a combination of environmental parameters (Brooks et al. 1994; Thompson et al. 2003; Doswell et al. 2012). Thus to better understand how environmental factors are related to the changes in the storms, we consider the combined effects of CAPE, CIN magnitude, and SRH. Figures 16–18 show phase space differences of CAPE and CIN (panels a–c of each figure) and CAPE and SRH (panels d–f) for the three events. Each shaded box in Figs. 16–18 represents differences in the number of grid points within the bounds of the box for the pre-industrial minus historical, mid-century minus historical, and late-century minus historical. The difference calculations in Figs. 16–18 use grid points where the most unstable CAPE is not zero and the maximum simulated reflectivity is less than 20 dBZ across all ensembles, the analysis domains in Fig. 1, and the analysis time periods in Table 1. We use the phase space approach over a composite parameter (e.g., energy helicity index) as it allows us to more clearly decompose the contributions of the individual parameters presented in the previous section.

We first look at the combined effects of CAPE, CIN magnitude, and SRH in the winter event (Fig. 16). The phase space differences indicate that the pre-industrial, mid-century, and late-century climates have more instances of favorable conditions for tornadic storms than in the historical climate. From Figs. 16a and 16d, the pre-industrial climate has more occurrences of high CAPE and SRH and low CIN than in the historical climate. The combined effect of these conditions suggests a more favorable environment for tornadic storm development in the pre-industrial when compared to the historical. From Figs. 16b,e and Figs. 16c,f, there is an increase in occurrences of high CAPE and SRH and low CIN from the historical to the mid- and late-century climates. Although an event like the winter tornadic storm is typically characterized

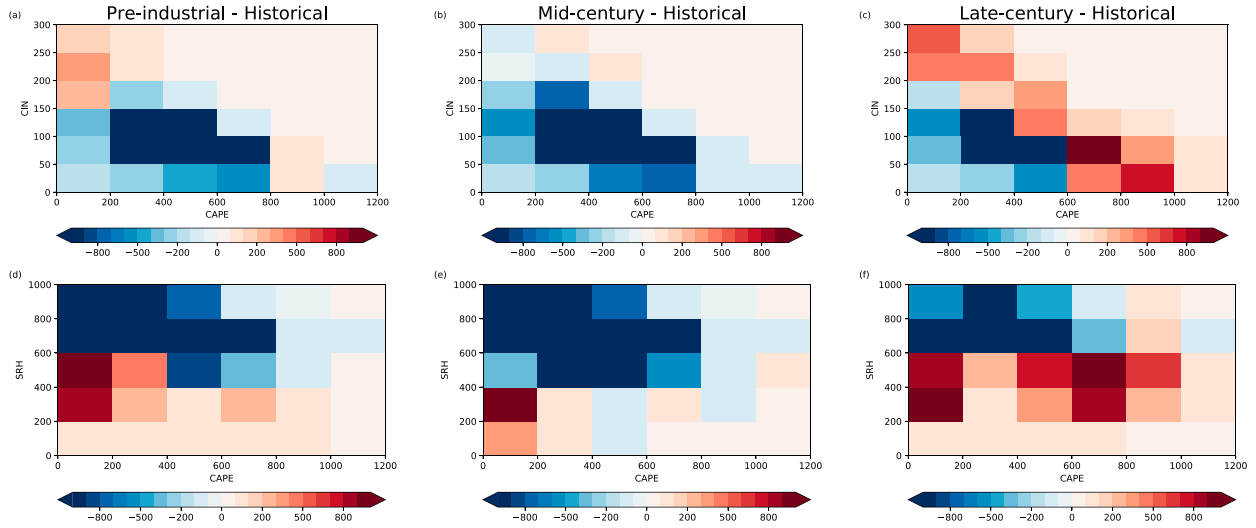


FIG. 17. As in Fig. 16, but for the (a),(d) pre-industrial minus historical, (b),(e) mid-century minus historical, and (c),(f) late-century minus historical from the nocturnal event near Nashville, TN.

by a low CAPE environment (Sherburn and Parker 2014), the combined effects of high CAPE and SRH and low CIN suggest that the future climate has a more favorable environment for tornadic storm development. The changes in favorability seen in Fig. 16 are consistent with Fig. 10a, where there is an increase in simulated storm activity in the past and future climates, with the largest increase seen in the late-century climate.

Next we look at the combined effects of CAPE, CIN magnitude, and SRH in the nocturnal event (Fig. 17). The phase space differences indicate that, compared to the historical climate, the pre-industrial and mid-century climates have less instances of favorable conditions while the late-century climate has more instances of favorable conditions. From Figs. 17a and 17d, the pre-industrial climate has an increase in high SRH and

low CAPE that often occur with high CIN when compared to the historical climate. The combined effect of these conditions, specifically the increase in CIN, suggests a less favorable environment for tornadic storm development in the pre-industrial climate. From Figs. 17b and 17e, there is an increase in high SRH and low CAPE, but there is also an increase in high CIN, suggesting that the mid-century climate is less favorable for tornadic storm development than in the historical climate. From Figs. 17c and 17f, the late-century climate shows an increase in occurrences of high CAPE and SRH and low CIN. Similar to the winter event, an event like the nocturnal tornadic storm is typically characterized by a low CAPE environment. However, the combined effects of the late-century high CAPE and SRH and low CIN suggest a future increase in favorability

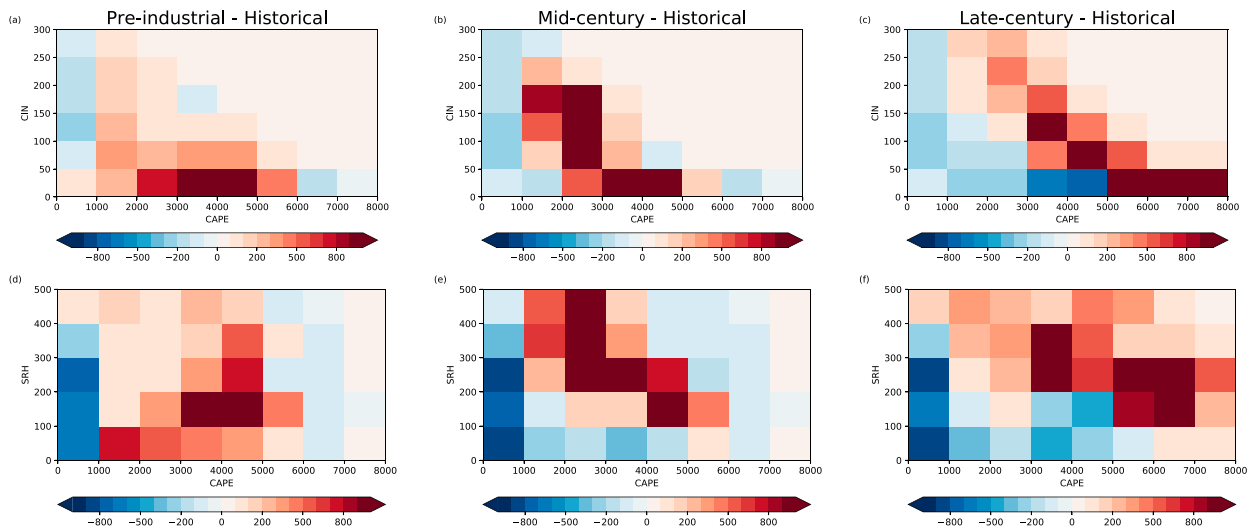


FIG. 18. As in Fig. 16, but for the (a),(d) pre-industrial minus historical, (b),(e) mid-century minus historical, and (c),(f) late-century minus historical from the spring event in Joplin, MO.

for rotating storms. The changes in favorability seen in Fig. 17 are also consistent with Fig. 10a, where there is a decrease in simulated storm activity in the pre-industrial and mid-century climates, and an increase in the late-century climate.

Finally, we look at the combined effects of CAPE, CIN magnitude, and SRH in the spring event (Fig. 18). The phase space differences indicate that the pre-industrial, mid-century, and late-century climates have the potential for more instances of favorable conditions for tornadic storms than the historical climate. From Figs. 18a and 18d, the pre-industrial climate has an increase in instances of high CAPE and SRH occurring with both low and high CIN compared to the historical climate. This suggests a possible increase in favorable conditions for tornadic storm development, although the increase in high CIN could result in reduced favorability. From Figs. 18b,e and Figs. 18c,f, the mid- and late-century climates have an increase in high CAPE and SRH that occur with both low and high CIN compared to the historical. While the occurrence of high CAPE and SRH with low CIN suggests more favorable conditions for tornadic storm development in the future climate, the potential for high CIN could also act to reduce the future favorability. In contrast to the winter and nocturnal events, the changes in favorability seen in Fig. 18 do not necessarily align with Fig. 10a, demonstrating that environmental parameters may not fully capture the climate-related changes affecting tornadic storms.

4. Conclusions and discussion

The effects of climate change on tornadic storms have proven difficult to determine and remain uncertain. In this study, we advance understanding of anthropogenic influences on tornadic storms by examining how historically impactful winter, nocturnal, and spring events could change in past and future climates. For each of the three tornadic storm events, we use five-member ensembles of convection-permitting hindcast simulations and adjust the initial and boundary conditions and greenhouse gas concentrations to represent the different climate states. Our analysis utilizes the updraft helicity (UH) and maximum simulated reflectivity to determine conditions indicative of tornadic storms, and large-scale parameters to assess the storm environments.

In the pre-industrial climate, our simulations of the winter event indicate an increase in storm activity compared to the historical climate. This increase is associated with moderate CAPE and high SRH in combination with low CIN. In contrast, our simulations of the nocturnal event indicate a decrease in storm activity in the pre-industrial climate compared to the historical climate. For the nocturnal event, the decrease is associated with a low-CAPE and high-SRH environment occurring with high CIN. In the spring event, the pre-industrial climate is mostly characterized by a high-CAPE and -SRH environment occurring with both low and high CIN. The variability in CIN makes it difficult to know if the potential for more robust storm development due to the high CAPE and SRH would actually come to fruition, or if the high CIN would suppress storms. However, the UH and maximum simulated reflectivity indicate that storm activity in our simulations of the

spring event decreases in the pre-industrial climate compared to the historical climate. This decrease may be due either to suppressed convective initiation from the high CIN or decreased lift due to other forcing mechanisms, such as fronts or other mesoscale boundaries, despite high CAPE. The uncertainty in interpreting the combined effects of the environmental parameters in the spring event highlights the complexity of understanding anthropogenic influences on tornadic storms and also demonstrates the problematic nature of solely using environmental parameters to examine these events.

In the future climate, our simulations of the winter event indicate an increase in storm activity compared to the historical climate, most notably in the late twenty-first century. This future increase is associated with the combined effects of high CAPE and SRH and low CIN in both the mid- and late-century climates. For the nocturnal event, our simulations indicate a decrease in storm activity in the mid-century climate compared to the historical climate, in association with low CAPE and SRH occurring with high CIN. In contrast, storm activity increases in the late-century climate, likely due to the combined effects of high CAPE and SRH occurring with low CIN. Although the simulated updrafts in winter in late-century climate and nocturnal events are not in proportion with the high CAPE, low CIN magnitudes likely create an environment conducive to robust supercell development. For the spring event, our simulations indicate an increase in storm activity in the mid-century climate consistent with an increase in occurrences of high CAPE and SRH, despite occurring within both low- and high-CIN environments. In the late-century climate, however, storm activity decreases, which suggests less convective initiation. This suppression of convective initiation is likely association with the high late-century CIN, despite high CAPE and SRH.

Our pseudo-global warming experiments allowed us to investigate three specific tornadic storm events under different climate states. The conclusions in this study are of course limited by the number of events, the model parameterizations, and the climate change deltas. This work, however, demonstrates that environmental parameters alone do not necessarily capture climate-related changes in supercell development. The response of tornadic storms to climate change is also likely very dependent on the season and diurnal timing of the event. Our results highlight the importance of examining winter and nocturnal tornadic storms, especially given their high fatality rates (Ashley et al. 2008). As the cases examined here demonstrate, the effects of future climate change have the potential to decrease spring and increase winter and nocturnal tornadic storms, which could lead to a dangerous increase in tornado vulnerability.

Acknowledgments. This material is based upon work supported by the U.S. Department of Defense, Environmental Security Technology Certification Program (ESTCP), under Project Number RC19-5264. This research used resources of the National Energy Research Scientific Computing Center (NERSC), a DOE Office of Science User Facility supported by the Office of Science of the U.S. DOE under Contract DE-AC02-05CH11231. All tornadic storm relevant variables were

calculated using WRF-Python (<https://doi.org/10.5065/D6W094P1>). We acknowledge the World Climate Research Programme, which, through its Working Group on Coupled Modelling, coordinated and promoted CMIP6. We thank the climate modeling groups for producing and making available their model output, the Earth System Grid Federation (ESGF) for archiving the data and providing access, and the multiple funding agencies who support CMIP6 and ESGF. We thank DOE's RGMA program area, the Data Management program, and NERSC for making this coordinated CMIP6 analysis activity possible. We thank three anonymous reviewers for their comments that have helped improve the paper.

Data availability statement. Climate model output is available on an open data portal (<https://portal.nersc.gov/archive/home/projects/cascade/www/Tornado>). We thank H. Krishnan for setting up the data portal on NERSC.

REFERENCES

- Allen, J. T., 2018: Climate change and severe thunderstorms. *Oxford Research Encyclopedia of Climate Science*, H. Brooks, Ed., Oxford University Press, <https://doi.org/10.1093/acrefore/9780190228620.013.62>.
- , D. J. Karoly, and K. J. Walsh, 2014: Future Australian severe thunderstorm environments. Part II: The influence of a strongly warming climate on convective environments. *J. Climate*, **27**, 3848–3868, <https://doi.org/10.1175/JCLI-D-13-00426.1>.
- Ashley, W. S., 2007: Spatial and temporal analysis of tornado fatalities in the United States: 1880–2005. *Wea. Forecasting*, **22**, 1214–1228, <https://doi.org/10.1175/2007WAF2007004.1>.
- , A. J. Krmenc, and R. Schwantes, 2008: Vulnerability due to nocturnal tornadoes. *Wea. Forecasting*, **23**, 795–807, <https://doi.org/10.1175/2008WAF2222132.1>.
- Berner, J., S.-Y. Ha, J. P. Hacker, A. Fournier, and C. Snyder, 2011: Model uncertainty in a mesoscale ensemble prediction system: Stochastic versus multiphysics representations. *Mon. Wea. Rev.*, **139**, 1972–1995, <https://doi.org/10.1175/2010MWR3595.1>.
- Brooks, H. E., 2013: Severe thunderstorms and climate change. *Atmos. Res.*, **123**, 129–138, <https://doi.org/10.1016/j.atmosres.2012.04.002>.
- , and C. A. Doswell III, 2001: Normalized damage from major tornadoes in the United States: 1890–1999. *Wea. Forecasting*, **16**, 168–176, [https://doi.org/10.1175/1520-0434\(2001\)016<0168:NDFMTI>2.0.CO;2](https://doi.org/10.1175/1520-0434(2001)016<0168:NDFMTI>2.0.CO;2).
- , —, and J. Cooper, 1994: On the environments of tornadic and nontornadic mesocyclones. *Wea. Forecasting*, **9**, 606–618, [https://doi.org/10.1175/1520-0434\(1994\)009<0606:OTEOTA>2.0.CO;2](https://doi.org/10.1175/1520-0434(1994)009<0606:OTEOTA>2.0.CO;2).
- , —, and M. P. Kay, 2003a: Climatological estimates of local daily tornado probability for the United States. *Wea. Forecasting*, **18**, 626–640, [https://doi.org/10.1175/1520-0434\(2003\)018<0626:CEOLDT>2.0.CO;2](https://doi.org/10.1175/1520-0434(2003)018<0626:CEOLDT>2.0.CO;2).
- , J. W. Lee, and J. P. Craven, 2003b: The spatial distribution of severe thunderstorm and tornado environments from global reanalysis data. *Atmos. Res.*, **67–68**, 73–94, [https://doi.org/10.1016/S0169-8095\(03\)00045-0](https://doi.org/10.1016/S0169-8095(03)00045-0).
- Carroll-Smith, D., R. J. Trapp, and J. M. Done, 2020: Exploring inland tropical cyclone rainfall and tornadoes under future climate conditions through a case study of Hurricane Ivan. *J. Appl. Meteor. Climatol.*, **60**, 103–118, <https://doi.org/10.1175/JAMC-D-20-0090.1>.
- Chen, F., and J. Dudhia, 2001: Coupling an advanced land surface–hydrology model with the Penn State–NCAR MM5 modeling system. Part I: Model implementation and sensitivity. *Mon. Wea. Rev.*, **129**, 569–585, [https://doi.org/10.1175/1520-0493\(2001\)129<0569:CAALSH>2.0.CO;2](https://doi.org/10.1175/1520-0493(2001)129<0569:CAALSH>2.0.CO;2).
- Coffer, B. E., M. D. Parker, R. L. Thompson, B. T. Smith, and R. E. Jewell, 2019: Using near-ground storm relative helicity in supercell tornado forecasting. *Wea. Forecasting*, **34**, 1417–1435, <https://doi.org/10.1175/WAF-D-19-0115.1>.
- , M. Taszarek, and M. D. Parker, 2020: Near-ground wind profiles of tornadic and nontornadic environments in the United States and Europe from ERA5 reanalyses. *Wea. Forecasting*, **35**, 2621–2638, <https://doi.org/10.1175/WAF-D-20-0153.1>.
- Colby, F. P., 1984: Convective inhibition as a predictor of convection during AVE-SESAME II. *Mon. Wea. Rev.*, **112**, 2239–2252, [https://doi.org/10.1175/1520-0493\(1984\)112<2239:CIAAPO>2.0.CO;2](https://doi.org/10.1175/1520-0493(1984)112<2239:CIAAPO>2.0.CO;2).
- Crook, N. A., 1996: Sensitivity of moist convection forced by boundary layer processes to low-level thermodynamic fields. *Mon. Wea. Rev.*, **124**, 1767–1785, [https://doi.org/10.1175/1520-0493\(1996\)124<1767:SOMCFB>2.0.CO;2](https://doi.org/10.1175/1520-0493(1996)124<1767:SOMCFB>2.0.CO;2).
- Danabasoglu, G., 2019: NCAR CESM2 model output prepared for CMIP6 CMIP. Earth System Grid Federation, accessed October 2019, <https://doi.org/10.22033/ESGF/CMIP6.2185>.
- Davies, J. M., 2017: Meteorological setting for a catastrophic event: The deadly Joplin tornado of 22 May 2011. *Electron. J. Severe Storms Meteor.*, **12** (3), <https://ejssm.org/ojs/index.php/ejssm/article/view/Article/164>.
- Davies-Jones, R., 1993: Helicity trends in tornado outbreaks. Preprints, *17th Conf. Severe Local Storms*, St. Louis, MO, Amer. Meteor. Soc., 56–60.
- Del Genio, A. D., M.-S. Yao, and J. Jonas, 2007: Will moist convection be stronger in a warmer climate? *Geophys. Res. Lett.*, **34**, L16703, <https://doi.org/10.1029/2007GL030525>.
- Diffenbaugh, N. S., R. J. Trapp, and H. E. Brooks, 2008: Does global warming influence tornado activity? *Eos, Trans. Amer. Geophys. Union*, **89**, 553–554, <https://doi.org/10.1029/2008EO530001>.
- , M. Scherer, and R. J. Trapp, 2013: Robust increases in severe thunderstorm environments in response to greenhouse forcing. *Proc. Natl. Acad. Sci. USA*, **110**, 16361–16366, <https://doi.org/10.1073/pnas.1307758110>.
- Done, J., C. A. Davis, and M. Weisman, 2004: The next generation of NWP: Explicit forecasts of convection using the Weather Research and Forecasting (WRF) model. *Atmos. Sci. Lett.*, **5**, 110–117, <https://doi.org/10.1002/asl.72>.
- Dong, Y., K. C. Armour, M. D. Zelinka, C. Proistosescu, D. S. Battisti, C. Zhou, and T. Andrews, 2020: Intermodel spread in the pattern effect and its contribution to climate sensitivity in CMIP5 and CMIP6 models. *J. Climate*, **33**, 7755–7775, <https://doi.org/10.1175/JCLI-D-19-1011.1>.
- Doswell, C. A., III, H. E. Brooks, and N. Dotzek, 2009: On the implementation of the enhanced Fujita scale in the USA. *Atmos. Res.*, **93**, 554–563, <https://doi.org/10.1016/j.atmosres.2008.11.003>.
- , G. W. Carbin, and H. E. Brooks, 2012: The tornadoes of spring 2011 in the USA: An historical perspective. *Weather*, **67**, 88–94, <https://doi.org/10.1002/wea.1902>.
- Duda, J. D., and W. A. Gallus, 2013: The impact of large-scale forcing on skill of simulated convective initiation and upscale evolution with convection-allowing grid spacings in the WRF. *Wea. Forecasting*, **28**, 994–1018, <https://doi.org/10.1175/WAF-D-13-00005.1>.
- Edwards, R., J. G. LaDue, J. T. Ferree, K. Scharfenberg, C. Maier, and W. L. Coulbourne, 2013: Tornado intensity estimation:

- Past, present, and future. *Bull. Amer. Meteor. Soc.*, **94**, 641–653, <https://doi.org/10.1175/BAMS-D-11-00006.1>.
- Eyring, V., S. Bony, G. A. Meehl, C. A. Senior, B. Stevens, R. J. Stouffer, and K. E. Taylor, 2016: Overview of the Coupled Model Intercomparison Project Phase 6 (CMIP6) experimental design and organization. *Geosci. Model Dev.*, **9**, 1937–1958, <https://doi.org/10.5194/gmd-9-1937-2016>.
- Frei, C., C. Schär, D. Lüthi, and H. C. Davies, 1998: Heavy precipitation processes in a warmer climate. *Geophys. Res. Lett.*, **25**, 1431–1434, <https://doi.org/10.1029/98GL51099>.
- Gallo, B. T., A. J. Clark, and S. R. Dembek, 2016: Forecasting tornadoes using convection-permitting ensembles. *Wea. Forecasting*, **31**, 273–295, <https://doi.org/10.1175/WAF-D-15-0134.1>.
- Geerts, B., and Coauthors, 2017: The 2015 Plains Elevated Convection at Night field project. *Bull. Amer. Meteor. Soc.*, **98**, 767–786, <https://doi.org/10.1175/BAMS-D-15-00257.1>.
- Gensini, V. A., and T. L. Mote, 2015: Downscaled estimates of late 21st century severe weather from CCSM3. *Climatic Change*, **129**, 307–321, <https://doi.org/10.1007/s10584-014-1320-z>.
- , C. Ramseyer, and T. L. Mote, 2014a: Future convective environments using NARCCAP. *Int. J. Climatol.*, **34**, 1699–1705, <https://doi.org/10.1002/joc.3769>.
- , T. L. Mote, and H. E. Brooks, 2014b: Severe-thunderstorm reanalysis environments and collocated radiosonde observations. *J. Appl. Meteor. Climatol.*, **53**, 742–751, <https://doi.org/10.1175/JAMC-D-13-0263.1>.
- Hoogewind, K. A., M. E. Baldwin, and R. J. Trapp, 2017: The impact of climate change on hazardous convective weather in the United States: Insight from high-resolution dynamical downscaling. *J. Climate*, **30**, 10081–10100, <https://doi.org/10.1175/JCLI-D-16-0885.1>.
- Iacono, M. J., J. S. Delamere, E. J. Mlawer, M. W. Shephard, S. A. Clough, and W. D. Collins, 2008: Radiative forcing by long-lived greenhouse gases: Calculations with the AER radiative transfer models. *J. Geophys. Res.*, **113**, D13103, <https://doi.org/10.1029/2008JD009944>.
- Janjić, Z. I., 1994: The step-mountain eta coordinate model: Further developments of the convection, viscous sublayer, and turbulence closure schemes. *Mon. Wea. Rev.*, **122**, 927–945, [https://doi.org/10.1175/1520-0493\(1994\)122<0927:TSMCEM>2.0.CO;2](https://doi.org/10.1175/1520-0493(1994)122<0927:TSMCEM>2.0.CO;2).
- Kain, J. S., and Coauthors, 2008: Some practical considerations regarding horizontal resolution in the first generation of operational convection-allowing NWP. *Wea. Forecasting*, **23**, 931–952, <https://doi.org/10.1175/WAF2007106.1>.
- Kerr, B. W., and G. L. Darkow, 1996: Storm-relative winds and helicity in the tornadic thunderstorm environment. *Wea. Forecasting*, **11**, 489–505, [https://doi.org/10.1175/1520-0434\(1996\)011<0489:SRWAHI>2.0.CO;2](https://doi.org/10.1175/1520-0434(1996)011<0489:SRWAHI>2.0.CO;2).
- Kis, A. K., and J. M. Straka, 2010: Nocturnal tornado climatology. *Wea. Forecasting*, **25**, 545–561, <https://doi.org/10.1175/2009WAF2222294.1>.
- Kunkel, K. E., X.-Z. Liang, J. Zhu, and Y. Lin, 2006: Can CGCMs simulate the twentieth-century “warming hole” in the central United States? *J. Climate*, **19**, 4137–4153, <https://doi.org/10.1175/JCLI3848.1>.
- Lackmann, G. M., 2013: The south-central U.S. flood of May 2010: Present and future. *J. Climate*, **26**, 4688–4709, <https://doi.org/10.1175/JCLI-D-12-00392.1>.
- , 2015: Hurricane Sandy before 1900 and after 2100. *Bull. Amer. Meteor. Soc.*, **96**, 547–560, <https://doi.org/10.1175/BAMS-D-14-00123.1>.
- Lawson, J. R., W. A. Gallus Jr., and C. K. Potvin, 2020: Sensitivity of a bowing mesoscale convective system to horizontal grid spacing in a convection-allowing ensemble. *Atmosphere*, **11**, 384, <https://doi.org/10.3390/atmos11040384>.
- Leibensperger, E. M., and Coauthors, 2012: Climatic effects of 1950–2050 changes in US anthropogenic aerosols—Part 2: Climate response. *Atmos. Chem. Phys.*, **12**, 3349–3362, <https://doi.org/10.5194/acp-12-3349-2012>.
- Marsh, P. T., H. E. Brooks, and D. J. Karoly, 2007: Assessment of the severe weather environment in North America simulated by a global climate model. *Atmos. Sci. Lett.*, **8**, 100–106, <https://doi.org/10.1002/asl.159>.
- Mauri, E. L., and W. A. Gallus Jr., 2021: Differences between severe and nonsevere warm-season, nocturnal bow echo environments. *Wea. Forecasting*, **36**, 53–74, <https://doi.org/10.1175/WAF-D-20-0137.1>.
- Meinshausen, M., and E. Vogel, 2016: input4MIPs.UoM.GHGConcentrations.CMIP.UoM-CMIP-1-2-0. Earth System Grid Federation, accessed October 2019, <https://doi.org/10.22033/ESGF/input4MIPs.1118>.
- Michaelis, A. C., J. Willison, G. M. Lackmann, and W. A. Robinson, 2017: Changes in winter North Atlantic extratropical cyclones in high-resolution regional pseudo-global warming simulations. *J. Climate*, **30**, 6905–6925, <https://doi.org/10.1175/JCLI-D-16-0697.1>.
- Molina, M. J., J. T. Allen, and A. F. Prein, 2020: Moisture attribution and sensitivity analysis of a winter tornado outbreak. *Wea. Forecasting*, **35**, 1263–1288, <https://doi.org/10.1175/WAF-D-19-0240.1>.
- Morrison, H., G. Thompson, and V. Tatarskii, 2009: Impact of cloud microphysics on the development of trailing stratiform precipitation in a simulated squall line: Comparison of one- and two-moment schemes. *Mon. Wea. Rev.*, **137**, 991–1007, <https://doi.org/10.1175/2008MWR2556.1>.
- NCDC, 2010: *Storm Data*. Vol. 52, No. 4, 384 pp.
- , 2011: *Storm Data*. Vol. 53, No. 5, 944 pp.
- Nijssen, F. J. M. M., P. M. Cox, and M. S. Williamson, 2020: An emergent constraint on transient climate response from simulated historical warming in CMIP6 models. *Earth Syst. Dyn. Discuss.*, 1–14, <https://doi.org/10.5194/esd-2019-86>.
- NOAA NCEI, 2019: Storm events database. Accessed October 2019, <https://www.ncdc.noaa.gov/stormevents/>.
- NWS, 2020: Weather related fatality and injury statistics. National Weather Service, accessed October 2019, <https://www.weather.gov/hazstat/>.
- O’Neill, B. C., and Coauthors, 2016: The Scenario Model Intercomparison Project (ScenarioMIP) for CMIP6. *Geosci. Model Dev.*, **9**, 3461–3482, <https://doi.org/10.5194/gmd-9-3461-2016>.
- Pan, Z., R. W. Arritt, E. S. Takle, W. J. Gutowski Jr., C. J. Anderson, and M. Segal, 2004: Altered hydrologic feedback in a warming climate introduces a “warming hole.” *Geophys. Res. Lett.*, **31**, L17109, <https://doi.org/10.1029/2004GL020528>.
- Patricola, C. M., and M. F. Wehner, 2018: Anthropogenic influences on major tropical cyclone events. *Nature*, **563**, 339–346, <https://doi.org/10.1038/s41586-018-0673-2>.
- Peters, J. M., H. Morrison, C. J. Nowotarski, J. P. Mulholland, and R. L. Thompson, 2020: A formula for the maximum vertical velocity in supercell updrafts. *J. Atmos. Sci.*, **77**, 3747–3757, <https://doi.org/10.1175/JAS-D-20-0103.1>.
- Potvin, C. K., and M. L. Flora, 2015: Sensitivity of idealized supercell simulations to horizontal grid spacing: Implications for warn-on-forecast. *Mon. Wea. Rev.*, **143**, 2998–3024, <https://doi.org/10.1175/MWR-D-14-00416.1>.

- Rasmussen, E. N., and D. O. Blanchard, 1998: A baseline climatology of sounding-derived supercell and tornado forecast parameters. *Wea. Forecasting*, **13**, 1148–1164, [https://doi.org/10.1175/1520-0434\(1998\)013<1148:ABCOSD>2.0.CO;2](https://doi.org/10.1175/1520-0434(1998)013<1148:ABCOSD>2.0.CO;2).
- Rasmussen, K. L., A. F. Prein, R. M. Rasmussen, K. Ikeda, and C. Liu, 2017: Changes in the convective population and thermodynamic environments in convection-permitting regional climate simulations over the United States. *Climate Dyn.*, **55**, 383–408, <https://doi.org/10.1007/s00382-017-4000-7>.
- Riahi, K., and Coauthors, 2017: The Shared Socioeconomic Pathways and their energy, land use, and greenhouse gas emissions implications: An overview. *Global Environ. Change*, **42**, 153–168, <https://doi.org/10.1016/j.gloenvcha.2016.05.009>.
- Robinson, E. D., R. J. Trapp, and M. E. Baldwin, 2013: The geospatial and temporal distributions of severe thunderstorms from high-resolution dynamical downscaling. *J. Appl. Meteor. Climatol.*, **52**, 2147–2161, <https://doi.org/10.1175/JAMC-D-12-0131.1>.
- Schär, C., C. Frei, D. Lüthi, and H. C. Davies, 1996: Surrogate climate-change scenarios for regional climate models. *Geophys. Res. Lett.*, **23**, 669–672, <https://doi.org/10.1029/96GL00265>.
- Seeley, J. T., and D. M. Romps, 2014: The effect of global warming on severe thunderstorms in the United States. *J. Climate*, **28**, 2443–2458, <https://doi.org/10.1175/JCLI-D-14-00382.1>.
- Sherburn, K. D., and M. D. Parker, 2014: Climatology and ingredients of significant severe convection in high-shear, low-CAPE environments. *Wea. Forecasting*, **29**, 854–877, <https://doi.org/10.1175/WAF-D-13-00041.1>.
- Shutts, G., 2005: A kinetic energy backscatter algorithm for use in ensemble prediction systems. *Quart. J. Roy. Meteor. Soc.*, **131**, 3079–3102, <https://doi.org/10.1256/qj.04.106>.
- Simmons, K. M., D. Sutter, and R. Pielke, 2013: Normalized tornado damage in the United States: 1950–2011. *Environ. Hazards*, **12**, 132–147, <https://doi.org/10.1080/17477891.2012.738642>.
- Skamarock, W. C., and Coauthors, 2008: A description of the advanced research WRF version 3. NCAR Tech. Note NCAR/TN-475+STR, 113 pp., <https://doi.org/10.5065/D68S4MVH>.
- Snively, D. V., and W. A. Gallus, 2014: Prediction of convective morphology in near-cloud-permitting WRF model simulations. *Wea. Forecasting*, **29**, 130–149, <https://doi.org/10.1175/WAF-D-13-00047.1>.
- Sobash, R. A., C. S. Schwartz, G. S. Romine, K. R. Fossell, and M. L. Weisman, 2016: Severe weather prediction using storm surrogates from an ensemble forecasting system. *Wea. Forecasting*, **31**, 255–271, <https://doi.org/10.1175/WAF-D-15-0138.1>.
- Taszarek, M., J. T. Allen, H. E. Brooks, N. Pilguy, and B. Czernecki, 2020: Differing trends in United States and European severe thunderstorm environments in a warming climate. *Bull. Amer. Meteor. Soc.*, **102**, E296–E322, <https://doi.org/10.1175/BAMS-D-20-0004.1>.
- Thompson, R. L., R. Edwards, J. A. Hart, K. L. Elmore, and P. Markowski, 2003: Close proximity soundings within supercell environments obtained from the Rapid Update Cycle. *Wea. Forecasting*, **18**, 1243–1261, [https://doi.org/10.1175/1520-0434\(2003\)018<1243:CPSWSE>2.0.CO;2](https://doi.org/10.1175/1520-0434(2003)018<1243:CPSWSE>2.0.CO;2).
- , C. M. Mead, and R. Edwards, 2007: Effective storm-relative helicity and bulk shear in supercell thunderstorm environments. *Wea. Forecasting*, **22**, 102–115, <https://doi.org/10.1175/WAF969.1>.
- , B. T. Smith, J. S. Grams, A. R. Dean, and C. Broyles, 2012: Convective modes for significant severe thunderstorms in the contiguous United States. Part II: Supercell and QLCS tornado environments. *Wea. Forecasting*, **27**, 1136–1154, <https://doi.org/10.1175/WAF-D-11-00116.1>.
- Tippett, M. K., J. T. Allen, V. A. Gensini, and H. E. Brooks, 2015: Climate and hazardous convective weather. *Curr. Climate Change Rep.*, **1**, 60–73, <https://doi.org/10.1007/s40641-015-0006-6>.
- Trapp, R. J., and K. A. Hoogewind, 2016: The realization of extreme tornadic storm events under future anthropogenic climate change. *J. Climate*, **29**, 5251–5265, <https://doi.org/10.1175/JCLI-D-15-0623.1>.
- , N. S. Diffenbaugh, H. E. Brooks, M. E. Baldwin, E. D. Robinson, and J. S. Pal, 2007: Changes in severe thunderstorm environment frequency during the 21st century caused by anthropogenically enhanced global radiative forcing. *Proc. Natl. Acad. Sci. USA*, **104**, 19719–19723, <https://doi.org/10.1073/pnas.0705494104>.
- , —, and A. Gluhovsky, 2009: Transient response of severe thunderstorm forcing to elevated greenhouse gas concentrations. *Geophys. Res. Lett.*, **36**, L01703, <https://doi.org/10.1029/2008GL036203>.
- , E. D. Robinson, M. E. Baldwin, N. S. Diffenbaugh, and B. R. J. Schwedler, 2011: Regional climate of hazardous convective weather through high-resolution dynamical downscaling. *Climate Dyn.*, **37**, 677–688, <https://doi.org/10.1007/s00382-010-0826-y>.
- University of Wyoming, 2020: Upper air sounding. Accessed March 2020, <http://weather.uwyo.edu/upperair/sounding.html>.
- Van Klooster, S. L., and P. J. Roebber, 2009: Surface-based convective potential in the contiguous United States in a business-as-usual future climate. *J. Climate*, **22**, 3317–3330, <https://doi.org/10.1175/2009JCLI2697.1>.
- Verbout, S. M., H. E. Brooks, L. M. Leslie, and D. M. Schultz, 2006: Evolution of the U.S. tornado database: 1954–2003. *Wea. Forecasting*, **21**, 86–93, <https://doi.org/10.1175/WAF910.1>.
- Weisman, M. L., W. C. Skamarock, and J. B. Klemp, 1997: The resolution dependence of explicitly modeled convective systems. *Mon. Wea. Rev.*, **125**, 527–548, [https://doi.org/10.1175/1520-0493\(1997\)125<0527:TRDOEM>2.0.CO;2](https://doi.org/10.1175/1520-0493(1997)125<0527:TRDOEM>2.0.CO;2).
- Yan, H., and W. A. Gallus, 2016: An evaluation of QPF from the WRF, NAM, and GFS models using multiple verification methods over a small domain. *Wea. Forecasting*, **31**, 1363–1379, <https://doi.org/10.1175/WAF-D-16-0020.1>.